



1 **Insights into the long-term (2005-2021) spatiotemporal evolution of** 2 **summer ozone production sensitivity in the Northern Hemisphere** 3 **derived with OMI**

4 Matthew S. Johnson^{1*}, Sajeev Philip², Scott Meech³, Rajesh Kumar³, Meytar Sorek-Hamer⁴, Yoichi P. Shiga⁴

5 ¹Earth Science Division, NASA Ames Research Center, Moffett Field, CA 94035, USA

6 ²Centre for Atmospheric Sciences, Indian Institute of Technology Delhi, New Delhi, India

7 ³Research Applications Laboratory, NSF National Center for Atmospheric Research, Boulder, CO 80305, USA

8 ⁴NASA Academic Mission Services by Universities Space Research Association at NASA Ames Research Center, Mountain
9 View, CA, USA

10 *Correspondence: Matthew S. Johnson (matthew.s.johnson@nasa.gov)

11 **Abstract.** Tropospheric ozone (O₃) formation depends on the relative abundance of precursor species, nitrogen oxides (NO_x) and
12 volatile organic compounds (VOCs). Advancements in satellite retrievals of formaldehyde (HCHO) and nitrogen dioxide (NO₂)
13 vertical column densities (VCDs), and the corresponding HCHO/NO₂ ratios (FNRs), provide the opportunity to diagnose the
14 spatiotemporal evolution of O₃ production sensitivity regimes. This study investigates trends of summertime VCD HCHO, NO₂,
15 and Ozone Monitoring Instrument (OMI) FNRs in the Northern Hemisphere from 2005 to 2021. FNR trends were analysed for
16 polluted regions, and specifically for 46 highly populated cities, over the entire 17-year period and in 2020 when global
17 anthropogenic emissions were reduced due to COVID-19 lockdown restrictions. It was determined that OMI-derived FNRs have
18 increased on average ~65% across cities in the Northern Hemisphere. Increasing OMI-derived FNRs indicates a general transition
19 from radical-limited to NO_x-limited regimes. The increasing trend is driven by reduced NO₂ concentrations because of emission
20 control strategies of NO_x. OMI FNR trends were compared to ground-based in situ measurements in US cities and determined they
21 can capture the trends in increasing FNRs (R = 0.91) and decreasing NO₂ (R = 0.98) occurring at the surface. OMI FNRs in urban
22 areas were higher (~20%) in 2020 for most cities studied here compared to 2019 and 2021. In addition to studying the longest
23 period of OMI FNRs across the Northern Hemisphere to-date, the capabilities and challenges of using satellite VCD FNRs to study
24 surface-level O₃ production sensitivity regimes are discussed.

25 **Short Summary.** Satellites, such as the Ozone Monitoring Instrument (OMI), retrieve proxy species of ozone (O₃) formation
26 (formaldehyde and nitrogen dioxide) and the ratios (FNRs) which can define O₃ production sensitivity regimes. Here we investigate
27 trends of OMI FNRs from 2005 to 2021 and they have increased in major cities suggesting a transition from radical- to nitrogen
28 oxide-limited regimes. OMI also observed the impact of reduced emissions during the 2020 COVID-lockdown resulting in
29 increased FNRs.

30 **1 Introduction**

31 Tropospheric ozone (O₃) is a harmful pollutant which has detrimental impacts on air quality leading to adverse human health and
32 premature mortality, and negative impacts on vegetation and agriculture (US EPA, 2006; Tai et al., 2014; GMD, 2020). A myriad
33 of volatile organic compounds (VOCs) can be photochemically oxidized through a complex series of chemical reactions involving
34 nitrogen oxides (NO_x = nitric oxide [NO] + nitrogen dioxide [NO₂]) which leads to tropospheric O₃ formation (Haagen-Smit, 1952;
35 Monks et al., 2015; Seinfeld and Pandis, 2016). The complex O₃-NO_x-VOC chemical relationship results in local nonlinear O₃
36 formation which is sensitivity to the relative abundances of its precursor species (NO_x and VOCs), generally categorized as “NO_x-
37 limited” versus “radical-limited” photochemical regimes (Sillman et al., 1990; Kleinman, 1994). In a NO_x-limited regime, local



38 O₃ production increases/decreases with increased/reduced NO_x emissions and concentrations, with no impact from VOC
39 perturbations. Whereas in a radical-limited regime (also known as “VOC-limited”, “hydrocarbon-limited”, or “NO_x-saturated”) the
40 formation of local O₃ increases/decreases with increased/reduced VOC emissions and concentrations; however, can also
41 slightly be impacted by NO_x emission and concentration changes. The accurate knowledge of regional and local O₃ photochemical
42 regimes is critical for developing emission control strategies to reduce surface O₃ concentrations. Overall, studying the
43 spatiotemporal evolution of the nonlinear O₃-NO_x-VOC chemistry is critical to policy decision making (National Research Council,
44 1991) and important as a fundamental scientific problem (Sillman, 1999).

45 Diagnosing regional and local O₃ photochemical regimes has always been recognized as a challenging task. Measurements
46 of proxy or indicator species (e.g., total reactive nitrogen, HCHO, hydrogen peroxide, nitric acid), and estimating the correlations
47 of such species, are the observation-based or model-observation synthesis approaches to detect O₃ sensitivity regimes (Sillman,
48 1995; Jacob et al., 1995; Tonnesen and Dennis, 2000). These measurements and associated studies are typically limited to field
49 campaign time periods and locations which hinders the spatiotemporal coverage of such data posing an obstacle for investigating
50 global and regional O₃ production sensitivity over multi-year time periods. The response of O₃ formation to changes in precursor
51 emissions can also be assessed through modeling approaches such as source apportionment studies (Li et al., 2012), forward model
52 sensitivity simulations (Wu et al., 2009), and simulations using adjoint model capabilities (Zhang et al., 2009). However,
53 uncertainties inherent in model predictions of O₃ physicochemical processes are an inherent issue. Milford et al. (1994) and Sillman
54 (1995) first introduced the concept of detecting photochemical regimes using the ratio of ambient concentrations of two “indicator
55 species” HCHO to NO₂ (hereafter indicator species refers to HCHO and NO₂; the ratio of these two species as FNR), which can
56 be used to represent VOCs and NO_x which are directly involved in O₃-NO_x-VOC chemistry and are readily measured via in situ
57 sampling and satellite remote-sensing techniques. These two indicator species are the most suitable candidates for tropospheric
58 column and planetary boundary layer (PBL) O₃ sensitivity analysis using satellites due to: 1) the sensitivity of nadir-looking
59 satellites to boundary layer FNRs, 2) most other indicator species (e.g., hydrogen peroxide, VOCs other than HCHO) cannot be
60 readily measured via satellites and the retrievals of those species having less sensitivity to surface conditions (e.g., limb-scanning
61 satellites), and 3) the short atmospheric lifetime of HCHO and NO₂ allowing these species to be suitable for proxies of surface
62 emissions of NO_x and VOCs.

63 Surface and PBL O₃ production sensitivity diagnosed with the in situ measurements of FNRs (although sparse in spatial
64 and temporal coverage) should be more accurate compared to satellite-based approaches of retrieving column-integrated
65 concentrations (Schroeder et al., 2017); however, the spatiotemporal coverage of polar orbiting satellites is a clear advantage over
66 in situ techniques. The advancements in satellite remote-sensing over the last two decades, to retrieve HCHO and NO₂ vertical
67 column density (VCD) data (Burrows et al., 1999; González Abad et al., 2019), have emerged as a new observation-based tool to
68 detect the spatiotemporal evolution of O₃ sensitivity from a global- to local-scale (Martin et al., 2004; Jin et al., 2020). Martin et
69 al. (2004) first demonstrated the capability of FNR VCDs from the Global Ozone Monitoring Experiment (GOME) satellite to
70 detect photochemical regimes. Subsequently, this technique was adopted by more studies using other satellite instruments such as
71 Ozone Monitoring Instrument (OMI), GOME-2, and TROPOspheric Monitoring Instrument (TROPOMI) (Duncan et al., 2010;
72 Witte et al., 2011; Choi et al., 2012; Choi and Souri, 2015; Chang et al., 2016; Jin and Holloway 2015; Souri et al., 2017; Jin et
73 al., 2017; 2020; Wang et al., 2021; Tao et al., 2022; Johnson et al., 2023; Acdan et al., 2023) up to a point that the results have
74 been suggested to potentially be used to inform State-Implementation Plans (SIP) in the United States (US) (Jin et al., 2018).
75 However, the accurate diagnosis of surface O₃ sensitivity regimes is impeded by numerous uncertainty components which can be
76 broadly classified into two major categories: 1) inherent uncertainties associated with the approach of relating indicator species to
77 diagnose local O₃ sensitivity at a location/time period, and 2) uncertainties associated with satellite-retrieved column-integrated



78 concentrations of indicator species to infer surface O₃ sensitivity. The former uncertainty arises from numerous factors: difficulties
79 in identifying accurate FNR “threshold” values (hereafter, “threshold” refers to threshold ratio values) separating different O₃
80 sensitivity regimes over a location and time period (Schroeder et al., 2017; Jin et al., 2017), dependency of ambient O₃ and its
81 formation to factors other than precursor species such as water vapor, meteorology, deposition, transport, and aerosol interaction
82 (e.g., Kleinman et al., 2005; Camalier and Dolwick, 2007), varying sensitivity of HCHO VCD data to anthropogenic VOCs (Jin et
83 al., 2020), and dependence of NO₂ in the production of ambient HCHO concentrations (Souri et al., 2020). These inherent
84 uncertainty sources limit the utility of satellite-based data for diagnosing O₃ sensitivity regimes. Fortunately, recent studies have
85 investigated these discrepancies in the methodology of using satellite-derived FNRs to infer O₃ sensitivity regimes using data from
86 airborne campaign data and 0-D photochemical box models (e.g., Schroeder et al., 2017; Souri et al., 2020; Souri et al., 2023a).

87 This study investigates 17 years (2005-2021) of OMI satellite sensor data which provides consistent near daily global
88 coverage of VCD retrievals of HCHO and NO₂ (Levelt et al., 2018) that are well suited to investigate the long-term spatiotemporal
89 evolution of O₃ sensitivity regimes. Numerous studies have used OMI VCD data up to the year 2016 to assess the trends in FNR
90 values over specific regions, mostly over the US and east Asia (Mahajan et al., 2015; Jin and Holloway, 2015; Souri et al., 2017;
91 Jin et al., 2017, 2020). Extending the OMI data set out to 2021 is novel and allows for the investigation of COVID-19 lockdown
92 restrictions on FNRs throughout the Northern Hemisphere. In this study we investigate the capability of VCD HCHO, NO₂, and
93 FNR data from OMI to reflect trends in PBL and surface level FNRs. We do not calculate actual magnitudes of surface HCHO,
94 NO₂, and FNRs derived with OMI VCD data as these proxy products are heavily reliant on chemical transport models (CTMs) and
95 spatiotemporally sparse ancillary information, both sources which have large uncertainties (discussed in Sect. 4). Satellite retrieval
96 errors can be reduced by averaging satellite data temporally (seasonal, annual, or multi-year means) and spatially (by averaging
97 individual satellite pixels across 10’s to 100’s of kilometers), although such averaging approaches preclude the analysis of O₃
98 sensitivity regimes at high spatiotemporal scales. Several studies have therefore focused on assessing O₃ production sensitivity
99 using spatially-averaged satellite data aggregated to monthly, seasonal, or multi-year means over large areas (e.g., Jin et al., 2020).
100 In this study, we investigate the long-term changes in summer-mean (June, July, and August [JJA]) VCD FNRs across numerous
101 polluted cities (cities with high NO₂ VCDs) in the Northern Hemisphere. This manuscript is structured in the following way.
102 Section 2 describes the OMI retrievals, surface concentration measurements, “bottom-up” emission inventories, and the approach
103 to conduct spatiotemporal variability and trend analysis. In Sect. 3, we describe the comparison of satellite VCD FNRs to surface
104 measurements and the analysis of OMI-derived FNR values over Northern Hemisphere cities. Section 4 discusses the capabilities
105 and issues with applying satellite-derived FNRs for studying O₃ production sensitivity and concluding remarks are provided in
106 Sect. 5.

107 2. Materials and methods

108 2.1 OMI satellite sensor

109 The OMI sensor is a Dutch-Finnish built payload on the NASA Earth Observing System Aura satellite. The Aura platform flies as
110 part of the Afternoon-Train satellite constellation along a sun-synchronous polar Low Earth Orbit (Schoeberl et al., 2006). Aura
111 passes through the sunlit part of the Earth 14 times a day with a local overpass time of ~1:45 p.m. at the equator with near-complete
112 daily global coverage (Levelt et al., 2006). OMI is a nadir-viewing solar backscatter grating spectrograph which takes retrievals in
113 the ultraviolet (264–311 nm [UV1] and 307–383 nm [UV2]) and visible (349–504 nm) wavelengths (Levelt et al., 2006, 2018;
114 Schenkeveld et al., 2017). The OMI instrument has a swath width of 2,600 km (60 pixels across track) with near-nadir spatial
115 resolution of 13 km (along-track) × 24 km (cross-track) and near-swath edge pixel size of 40 km × 250 km. OMI has been widely
116 used by the atmospheric science, air quality, and health impact assessment communities since its launch on July 15, 2004 (e.g.,



117 Levelt et al., 2018). The “row anomaly” appeared starting in May 2007 affecting the data quality of certain rows of OMI pixels
118 (Dobber et al., 2008, Schenkeveld et al., 2017) and is avoided in the data products used in this study.

119 **2.1.1 OMI HCHO**

120 This study applies the NASA-released operational OMI HCHO version 3 collection 3 (OMHCHO) gridded level 3 (L3) VCD data
121 at a spatial resolution of $0.1^\circ \times 0.1^\circ$ latitude \times longitude using the Smithsonian Astrophysical Observatory (SAO) retrieval
122 algorithm (González Abad et al., 2015). The OMHCHO retrieval applies a nonlinear fitting to the OMI-measured backscattered
123 radiances in the UV2 spectral window following the Basic Optical Absorption Spectroscopy method (Chance, 1998) to get slant
124 column densities (SCDs). The SCDs are then converted to VCDs by applying the air mass factor (AMF) formulation of Palmer et
125 al. (2001), with scattering weights calculated using the Linearized Discrete Ordinate Radiative Transfer version 2.4RT (VLIDORT)
126 Radiative Transfer Model (RTM) (Spurr, 2006) and HCHO shape factors simulated using the GEOS-Chem global CTM at a spatial
127 resolution of $2^\circ \times 2.5^\circ$ latitude \times longitude. The OMHCHO VCD product has a postprocessing bias correction (De Smedt et al.,
128 2008) applied by comparing daily HCHO VCDs with background VCDs simulated with GEOS-Chem over a clean region in the
129 Pacific Ocean (González Abad et al., 2015). González Abad et al. (2015) estimated the uncertainty of the OMHCHO product
130 ranging from 45% to 105%, with relative contributions from the slant column retrievals (45% – 100%) and AMF calculations
131 (~35%). Validation of OMHCHO with aircraft-based observations indicate a high bias (66.1% – 112.1%) for HCHO-poor
132 environment and low bias (-44.5% – -21.7%) for HCHO-rich environments (Zhu et al., 2016, 2020; Johnson et al., 2023). The
133 OMHCHO product has been used widely for estimating trends of VOC emissions (e.g., Marais et al., 2012; Shen et al., 2019) and
134 inferring surface HCHO concentrations (Zhu et al., 2017a).

135 **2.1.2 OMI NO₂**

136 The NASA-released standard OMI NO₂ (OMNO2) version 4 collection 3 gridded L3 high resolution VCD data at the spatial
137 resolution of $0.1^\circ \times 0.1^\circ$ latitude \times longitude was applied in this study (Lamsal et al., 2015; Krotkov et al., 2017). The OMNO2
138 retrieval uses the Differential Optical Absorption Spectroscopy method (Marchenko et al., 2015) to derive tropospheric SCDs by
139 spectrally fitting OMI-detected backscattered radiance in the visible wavelength window with a pseudo reference spectrum
140 (Chance and Spurr, 1997). The stratospheric contribution of the SCD is then subtracted and the residual tropospheric SCDs are
141 then converted to tropospheric VCDs by applying an AMF based on scattering weights calculated using the Total Ozone Mapping
142 Spectrometer (TOMS) radiative transfer model (TOMRAD) (Dave, 1964) and shape factor profiles simulated using the Global
143 Modeling Initiative (GMI) CTM at a spatial resolution of $1^\circ \times 1.25^\circ$ latitude \times longitude (Krotkov et al., 2017). The uncertainty of
144 the OMNO2 VCD product varies with cloudiness and pollution levels but is in the range of ~20% – 60% (Bucsela et al., 2013),
145 with relative contributions from the spectral fitting (~10% over polluted regions, Boersma et al., 2011), stratospheric correction
146 (<5%), and AMF calculations (10% – 20%). The OMNO2 product has been used for a wide range of applications including the
147 estimation of spatiotemporal variability and trends of NO_x emissions (e.g., Krotkov et al., 2016), NO₂ surface concentrations (e.g.,
148 Kharol et al., 2015; Lamsal et al., 2015), information about atmospheric particulate organic matter (Philip et al., 2014), and surface
149 O₃ sensitivity regime detections (e.g., Duncan et al., 2010; Jin et al., 2017).

150 **2.1.3 Calculation of VCD FNR values**

151 The daily L3 OMHCHO and OMNO2 products were filtered and processed for calculating FNR values. Both the operational
152 products were already filtered for daily VCDs with an effective cloud fraction >30%, solar zenith angle >70% (for HCHO) and
153 >85% (for NO₂), removing pixels affected by row anomalies, and Level 2 data quality flags not designated as good (see more



154 details in the user's guides for OMNO2 [https://disc.gsfc.nasa.gov/datasets/OMNO2d_003/summary] and OMHCHO
155 [https://acdisc.gesdisc.eosdis.nasa.gov/data/Aura_OMI_Level3/OMHCHOd.003/doc/README_OMHCHOd_v003.pdf]).
156 During this study, we avoided unrealistically large positive and negative values for both indicator species which occur due to
157 uncertainties in slant column retrievals and the calculation of tropospheric VCDs. We followed Zhu et al. (2020) to filter out HCHO
158 daily VCDs outside the range of -8.0×10^{15} molecules cm^2 to 7.6×10^{16} molecules cm^2 . The OMNO2 L3 product already included
159 an upper limit of 1×10^{17} molecules cm^2 and we applied a lower limit of -1×10^{15} molecules cm^2 below which NO_2 VCD are
160 assumed in this study to be unrealistic. After data filtering, OMI VCD FNRs are calculated by taking the ratio of HCHO: NO_2 for
161 each grid of the summer-mean products.

162 2.2 Surface measurement data

163 To determine if OMI VCD FNRs can replicate the trends of PBL and surface-level FNRs, long-term trends in OMI-derived VCD
164 HCHO and NO_2 are compared to in situ measurement data from the United States Environmental Protection Agency's Air Quality
165 System (US EPA AQS; <https://www.epa.gov/aqs>). We focus this evaluation on the US due to the much denser in situ measurement
166 networks compared to other global regions. Hourly data from the EPA AQS NO_2 data were averaged daily from 1 pm to 3 pm
167 local time to be consistent with the OMI overpass time. Since there are insufficient hourly data for HCHO from the EPA AQS
168 network, we use 24-hour average data for the HCHO evaluation. Valid and continuous data points were then averaged to obtain
169 seasonal summertime mean (JJA) values from 2005 to 2019 to be intercompared with corresponding OMI VCD values.

170 The AQS NO_2 data suffers from potential interference of reactive nitrogen species while measuring NO converted from
171 NO_2 in molybdenum catalytic converters, since other reactive species also get converted to NO. We attempted to account for this
172 interference by applying a model simulated correction factor (CF; Eq. 1) to the raw AQS data, following the approach of previous
173 studies (Lamsal et al., 2008; 2010; Cooper et al., 2020).

$$174 \quad CF = \frac{NO_2}{NO_2 + (0.15 \times HNO_3) + (0.95 \times PAN) + \text{Alkyl Nitrates}} \quad (1)$$

175 The CF is calculated using the MERRA2-GMI simulated concentrations of NO_2 , HNO_3 , peroxyacetyl nitrate (PAN), and alkyl
176 nitrates, and by applying an assumed effective conversion efficiency of 15% for HNO_3 and 95% for PAN (see Lamsal et al., 2010).
177 The AQS's method to measure HCHO is affected by interference from species such as O_3 and NO_2 and since there is insufficient
178 information to correct those interferences, here we use uncorrected AQS HCHO data.

179 2.3 Surface emissions of NO_x

180 To compare the long-term evolution of FNRs with human-induced changes in precursor emissions (anthropogenic emissions of
181 NO_x), we used the most recent Community Emissions Data System (CEDS v_2021_04_21) NO_x bottom-up emission data set
182 (McDuffie et al., 2020). As explained in the results section of this manuscript, we focus our analysis on trends in NO_x emission
183 instead of HCHO as it was determined that trends in NO_2 concentrations clearly drive the global trends in FNRs. The CEDS data
184 provides monthly anthropogenic NO_x emissions at $0.5^\circ \times 0.5^\circ$ horizontal spatial scales from 1750 – 2019. For this study we analyse
185 trends in anthropogenic NO_x emissions (source sectors: Agriculture; 1: Energy; 2: Industrial; 3: Transportation; 4: Residential,
186 Commercial, Other; 5: Solvents production and application; 6: Waste; 7: International Shipping) between 2005 – 2019 to overlap
187 with OMI observations. We used mean emissions for summer months (JJA) for each year to intercompare with OMI derived NO_2
188 and FNR trends. Since our focus in this study was to assess the overall relationship of long-term changes in OMI-derived FNR
189 values and corresponding changes in the anthropogenic NO_x over a city/region, we do not consider other natural sources (e.g.,
190 biomass burning) contributing to ambient concentrations of NO_2 .



191 2.4 Spatiotemporal analysis of FNRs

192 The spatiotemporal analysis of OMI-derived VCD NO₂ and HCHO values was conducted as follows. First, summer-mean trends
193 from 2005 to 2021 of HCHO and NO₂ VCDs and FNR values were calculated at the native spatial resolution (0.1° × 0.1°). Long-
194 term trends were calculated for each grid of HCHO, NO₂, and FNRs with ordinary least-squares linear regression (at various
195 confidence levels calculated with the Mann-Kendall Test) similar to past studies (e.g., Boys, et al., 2014; Kharol et al., 2015;
196 Geddes et al., 2016). To reduce retrieval random errors and improve precision, we focus on summer-mean data for each year and
197 multi-year means (three multi-year means: 2005 – 2010, 2011 – 2015 and 2016 – 2021) around 46 cities across the Northern
198 Hemisphere. The focus on the summer season was also chosen to utilize HCHO VCD retrievals with significantly better signal to
199 noise ratios compared to winter, spring, and fall months. High levels of surface HCHO concentrations over source regions form
200 due to the higher oxidant availability in summer (González Abad et al., 2015; Zhu et al., 2014; 2017a; 2017b) which leads to better
201 retrievals of HCHO VCDs. We restrict our analysis to the Northern Hemisphere as most continental polluted regions exist there.
202 We assessed the evolution of FNRs over urban and rural/suburban (hereinafter referred to just as rural) areas around cities. To
203 define urban city regions, we used the hybrid dataset, CGLC-MODIS-LCZ (Demuzere et al., 2023), which is based on the
204 Copernicus Global Land Service Land Cover (CGLC) product resampled to MODIS IGBP classes (CGLC-MODIS) and the global
205 map of Local Climate Zones (LCZ) (Stewart and Oke., 2012) that describe the heterogeneous urban land surface. This data set was
206 interpolated onto a 0.1° × 0.1° grid to match the resolution of the L3 OMI satellite data. Urban classification is defined by the
207 CGLC-MODIS-LCZ land use categories 51 – 60, which includes a range of urban land use from sparsely built to compact high-rise
208 including the heavy industry category. Rural grids are those not defined as urban and within 7 × 7 grid boxes of the city center.

209 In this study, we focus only on the spatiotemporal variability of indicator ratios, rather than the exact ozone sensitivity
210 regimes which can be inferred from these ratios. Although several previous studies assigned ratio values to certain O₃ regimes
211 (e.g., Jin et al., 2017; Souri et al., 2017) based on previous modelling and limited-observational studies, large uncertainty exists in
212 the classification of O₃ regimes using FNR values (Schroeder et al., 2017; Jin et al., 2020; Souri et al., 2021). Nevertheless,
213 whenever the ratio values were assessed over a city/region, we also presented the threshold ratio values (separating O₃ regimes)
214 suggested by Jin et al. (2020) for some cities in the US (Los Angeles, New York, Chicago, Washington DC, Pittsburgh, Atlanta
215 and Houston), Wang et al. (2021) for cities in China, and Duncan et al. (2010) for all other cities/regions. Note that the threshold
216 FNR values (< 1 as radical-limited versus > 2 as NO_x-limited) suggested by Duncan et al. (2010) is a crude approximation as
217 opposed to more recent and observationally-constrained threshold ratio values suggested by Jin et al. (2020) and Wang et al. (2021).
218 We believe that an accurate classification of O₃ regimes is still an ongoing research topic (Schroeder et al., 2017; Jin et al., 2020;
219 Souri et al., 2021) which should be addressed in future studies.

220 3. Results

221 3.1 Long-term mean OMI data

222 Figure 1 shows the long-term mean (2005-2021) maps of OMI-derived VCDs of HCHO and NO₂ and the corresponding column
223 FNR values. Formaldehyde enhancements reflect surface emissions of anthropogenic VOC (densely populated regions in China;
224 Shen et al., 2019), biogenic isoprene (southeast US; Millet et al., 2008), and biomass burning (South Asia; Mahajan et al., 2015).
225 OMI VCD NO₂ is abundant over urban areas primarily due to combustion emissions from traffic (Duncan et al., 2015) and over
226 regions with large industrial activities (Krotkov et al., 2016). The column FNRs clearly reveal lower values over cities (FNR < 2),
227 marginal values over rural/suburban regions surrounding large cities (FNR in the range of 2 - 5), and higher values elsewhere (FNR
228 > 5). The lower FNRs over cities suggest radical-limited conditions, and larger FNR values in non-polluted background regions



229 reflect NO_x -limited conditions (Martin et al., 2004; Duncan et al., 2010; Jin et al., 2017; 2020; Wang et al., 2021). Lower FNR
230 values retrieved by OMI are most noticeable in the highly populated regions of the US (e.g., Los Angeles, New York, Chicago),
231 Europe (e.g., London, Amsterdam, Paris), east Asia (e.g., Beijing, Shanghai, Jinan), and Middle East (e.g., Dubai, Tehran, Riyadh)
232 where tropospheric column NO_2 abundances are enhanced. The highest FNR values are observed in regions of the southeast US
233 and south Asia where there are no large cities and enhanced tropospheric column HCHO abundances are observed.

234 3.2 Capability of OMI VCD data to observe surface-level FNR trends

235 Before assessing VCD FNR trends, we compared trends in OMI NO_2 and HCHO VCD data, and corresponding tropospheric
236 column FNRs, to surface in situ measurements from EPA AQS in the US in order to determine whether OMI VCD information
237 tracks trends occurring at the surface. Figure 2 shows the 15-year time-series (2005-2019) comparison between normalized time
238 series of OMI VCD indicator species abundances and FNRs and AQS data over select cities (US cities with continuous AQS data),
239 and over all cities averaged across the continental US (USA, 373 separate sites). Table 1 shows the correlation between OMI VCD
240 and AQS in situ NO_2 , HCHO, and FNR summer mean values in addition to the simple linear regression slope of normalized trends
241 from OMI and AQS for both indicator species and FNRs. Figure 2 shows that both OMI VCD and in situ AQS data have relatively
242 neutral trends in HCHO between 2005 and 2019 for most of the large urban cities of the US. While there is large interannual
243 variability in HCHO concentrations, the long-term trends are relatively flat. On average, the normalized linear trends in surface
244 HCHO was -0.05 and OMI VCDs was 0.15. OMI VCD HCHO data is unable to replicate the interannual variability and long-term
245 trends of surface data displayed by the low correlation values and opposing trends in multiple large cities in the US. The inability
246 of OMI to reflect the variability in HCHO observed at the surface is likely due to the large noise in OMI HCHO retrievals (e.g.,
247 Johnson et al., 2023, Souri et al., 2023a) and complex vertical distributions of HCHO complicating satellite retrievals and
248 understanding surface values (e.g., Souri et al., 2023b).

249 OMI VCD and in situ AQS data of NO_2 display a different story where significant reductions in NO_2 concentrations are
250 observed by both data sources. The normalized trends in NO_2 from both measurement platforms are in strong agreement (see Fig.
251 2 and Table 1). Correlation between OMI VCD and AQS NO_2 were near unity ($R=0.98$) and both data sources had normalized
252 linear regression slopes of ~ -0.20 . This suggests that OMI is able to observe the strong reduction in NO_2 concentrations at the
253 surface measured by AQS across the US. Both data sources suggest that NO_2 reduced between 2005-2019 and the strongest
254 negative trends were in the large cities of the US such as New York, Chicago, and Los Angeles. The near neutral trend in HCHO
255 and large decreases in NO_2 results in both OMI VCD and in situ data sources observing an increasing trend in FNR data in all
256 major cities of the US shown in Fig. 2. The normalized linear regression trend slopes of FNRs (0.21 from both OMI and AQS data)
257 are nearly equal and opposite to NO_2 , suggesting the reduction of NO_2 is the primary driver of FNR trends over time. It is
258 encouraging that OMI VCD data is able to accurately reproduce the normalized trends in surface FNRs in the US. This agrees with
259 the recent studies from Jin et al. (2017) and Souri et al. (2023a) which show that ratios of mid-day VCD FNRs to PBL and surface-
260 level concentrations are near unity. Since OMI VCD FNRs appear to be able to replicate the trends in surface FNRs, the rest of
261 this study focuses on the trends of FNRs from OMI VCD data for the Northern Hemisphere.

262 3.3 17-year trend in OMI observations

263 This study investigates the 17-year trend of OMI VCD of HCHO, NO_2 and FNR values between 2005 and 2021. Figure 3 shows
264 the long-term trend in OMI VCD HCHO, NO_2 and FNR values at an 85% confidence level ($p \leq 0.15$) (Fig. S1 shows the same
265 trend values at a 99% [$p \leq 0.01$] confidence level and for all grid cells with OMI retrievals). Formaldehyde VCDs increased by
266 $\sim 0.5 \times 10^{14}$ molecules $\text{cm}^{-2} \text{yr}^{-1}$ over most of the Northern Hemisphere, with reductions up to $\sim 0.5 \times 10^{14}$ molecules $\text{cm}^{-2} \text{yr}^{-1}$ over



267 the southeast US. This trend is consistent with previous studies documenting increases in multi-satellite (including OMI) summer
268 mean HCHO over Northern China (during 2005-2016 [Shen et al., 2019] and 2005-2014 [Souri et al., 2017]) and increases in most
269 regions in the US (during 2005-2014 [Zhu et al., 2017b]) due to increasing anthropogenic VOC emissions. Some near neutral
270 trends, to small decreases, are seen in Fig. 3 in eastern China. The decrease in HCHO over Southern China could be due to
271 reductions in anthropogenic VOCs (Souri et al., 2017; Itahashi et al., 2022) or biogenic VOC emissions as noted by Jin and
272 Holloway (2015). The decreases in summer mean OMI HCHO over the southeast US was also documented in earlier studies (De
273 Smedt et al. 2015; Zhu et al., 2017b). Note that the trend in HCHO calculated in this study is influenced by yearly variations in
274 temperature, in contrast to Shen et al. (2019) and Zhu et al. (2017b) that corrected for the impact of varying temperature on HCHO
275 VCDs.

276 The negative trend in NO₂ OMI VCDs over populated regions of the US, Europe, and eastern China, and increases in the
277 South Asia and Middle East regions, seen in Fig. 3 are consistent with several previous studies (e.g., Hilboll et al., 2013; Jin et al.,
278 2017). The decreases in eastern China and Europe are as large as -2.0×10^{14} molecules cm⁻² yr⁻¹ while reductions in NO₂ in the
279 US are between -0.1 to -1.0×10^{14} molecules cm⁻² yr⁻¹. The decreasing NO₂ trend in eastern China could be due to recent reductions
280 in anthropogenic NO_x emissions after year 2011 (e.g., Fan et al., 2021). It is well demonstrated that the tropospheric NO₂ decreases
281 in most Northern Hemisphere regions, particularly in urban regions, is due to reductions in anthropogenic NO_x emissions
282 implemented through national governmental policies (e.g., Duncan et al., 2016). Figure S2 shows the trends in CEDS
283 anthropogenic NO_x emissions between 2005-2019 which have nearly identical regions of reduction as those retrieved by OMI
284 NO₂. Overall, the summer-mean trend in VCD NO₂ estimated in this study is generally consistent with the reported satellite-based
285 annual mean surface NO₂ trend estimated on a global-scale (Geddes et al., 2015) and over the US (Kharol et al., 2015; Lamsal
286 et al., 2015).

287 The most notable feature in Fig. 3 is the general increasing trend in OMI VCD FNR values over most of the polluted
288 regions in the Northern Hemisphere. The increasing OMI column FNR values suggest a trend towards more NO_x-limited regimes
289 around cities in recent years which has been noted by some previous studies (Jin et al., 2017; 2020; Souri et al., 2017). Increases
290 in FNRs in the populated regions of China, Europe, and US reach values between 0.1 and 0.2 yr⁻¹. The increases in FNRs are
291 driven mostly by the reductions in NO₂ rather than the small variations in HCHO, as evident in Fig. 2 and 3. The following sections
292 focus on the assessment of the evolution of summer mean OMI-derived VCD FNRs over numerous selected cities in the Northern
293 Hemisphere.

294 **3.4 Evolution of OMI FNRs around populated cities in the Northern Hemisphere**

295 Figure 4 shows the time series of summer mean OMI VCD FNRs from 2005 to 2021 over 18 selected large cities. The
296 corresponding normalized time series trends of OMI-derived NO₂ abundances and FNRs, and CEDS anthropogenic emissions of
297 NO_x over these cities, are displayed in Fig. 5. From Fig. 4 it can be seen that the largest positive trends in OMI FNRs during the
298 2005-2021 time period occurred over three mega-cities in the US: Los Angeles, New York and Chicago. Time series of the actual
299 magnitudes of OMI VCD NO₂ and HCHO abundances over the selected 18 large cities are shown in Fig. S3. In addition to increases
300 in FNRs in US cities, relatively large increases in FNRs are also evident in European (e.g., London) and Asian (e.g., Guangzhou)
301 cities. Figure 5 reveals that the increases in OMI FNR values over the selected 18 mega-cities are linked with decreases in NO₂
302 abundances due to reductions in anthropogenic NO_x emissions. The spatial map of trends in CEDS anthropogenic emissions of NO_x
303 across the Northern Hemisphere between 2005-2019 are shown in Fig. S2 (timeseries of CEDS NO_x emission magnitudes for the
304 selected 18 mega-cities shown in Fig. S4). Based on the O₃ production sensitivity regime thresholds suggested by Jin et al. (2020)
305 (note that these thresholds are applicable for VCD data), all the US cities shown in Fig. 4 that were VOC-limited in the early 2000's



306 show clear transition towards NO_x -limited and transitional regimes in recent years. Major cities in Europe such as London and
307 Amsterdam have also experienced increasing FNRs moving from VOC-limited regimes to transitional, or even NO_x -limited,
308 regimes in recent years (based on thresholds from Duncan et al. [2010]). Increases in the magnitudes of FNRs were generally
309 smaller in large cities of Asia; however, only Neijiang doesn't display some noticeable increases in FNRs in recent years. In
310 Neijiang, CEDS anthropogenic NO_x emissions are decreasing after 2012; however, OMI does not retrieve decreasing NO_2
311 abundances leading to the near-neutral trend in FNR values. Based on the O_3 production sensitivity regimes thresholds defined by
312 Wang et al. (2021) and Duncan et al. (2010), major cities in Asia have FNR values which are in the transitional or NO_x -limited
313 regimes in recent years besides Beijing, Shanghai, Jinan, and Riyadh (surrounding rural region is in the transitional regimes) (see
314 Fig. 4). Figure 5 shows these large Asian cities, besides Riyadh, implemented NO_x emission control strategies in ~2012 and have
315 recent negative trends in OMI NO_2 ; however, based on Wang et al. (2021) these urban regions have O_3 production which is still
316 limited by VOCs. Overall, it is difficult to conclude if these major cities in the Northern Hemisphere have in fact transitioned to
317 NO_x -limited and transitional regimes due to the large uncertainties in the exact threshold FNR values which separate these chemical
318 regimes.

319 In the vast majority of cities between 2005-2021 OMI retrieved larger FNR values in the rural regions surrounding urban
320 regions in the Northern Hemisphere compared to the urban city centers. Figure 6 shows spatial maps of OMI-derived VCD FNRs
321 around the selected 18 cities discussed above for two 6-year averages: 2005-2010 and 2015-2021 reflecting the earliest and most
322 recent years of OMI data studied here. This figure shows that OMI is able to retrieve the differences in FNRs in urban and rural
323 regions surrounding large cities in the Northern Hemisphere. In urban areas of cities, where emission sources of NO_x are largest,
324 OMI FNRs tend to be lower indicating more tendency towards VOC-sensitive O_3 production regimes compared to the surrounding
325 rural regions. This figure also displays the decadal-scale changes (2016–2021 versus 2005–2010) in the OMI FNRs over the
326 Northern Hemisphere urban regions and surrounding rural regions. In all 18 cities FNR values increase in both rural and urban
327 areas with noticeable increases in the spatial coverage of potentially NO_x -limited O_3 production regimes. Large cities in the US
328 show the clearest increase in the spatial coverage of potentially NO_x -limited O_3 production regimes; however, European and Asian
329 cities also follow a similar pattern with less increase in FNR magnitude overall. Recent studies have also noted that NO_x -limited
330 regimes have expanded spatially into the city centers, on a decadal-scale, throughout the Northern Hemisphere (Jin et al., 2017)
331 and in the US (Jin et al., 2020). This has large implications for O_3 sensitivity analysis and development of future emission control
332 strategies for improving air quality.

333 Figure 7 shows the changes in OMI FNRs (multi-year averaged values: 2005-2010, 2011-2015, and 2016-2021) over 46
334 cities in the Northern Hemisphere. The vast majority of urban regions in the Northern Hemisphere (44 of the 46 selected cities)
335 experienced increasing FNRs between 2005-2010 and 2016-2021. OMI FNRs for Tehran, Iran and Neijiang, China were two
336 selected cities which did not display increasing values. On average, FNRs in urban areas of the selected cities increased by ~65%
337 between 2005-2010 and 2016-2021. Similar to urban regions, the vast majority of rural regions surrounding urban areas in the
338 Northern Hemisphere (44 of the 46 selected cities) experienced increasing FNRs between 2005-2010 and 2016-2021. The average
339 increase of FNRs in the rural regions increased slightly less (~38%) compared to urban areas. In agreement with results discussed
340 above, FNR values in rural regions are larger compared to city centers. However, OMI VCD FNR differences between rural and
341 urban regions were reduced by ~15% on average over the 17-year time period. This suggests that the urban/rural interface of FNRs
342 is becoming less drastic and NO_x -limited O_3 production regimes that in the past were predominantly observed in rural regions have
343 expanded into the urban regions of larger cities. More accurate assessment of the actual threshold ratio values separating the
344 different O_3 production regimes would allow for the determination of exactly what extent of each city has in fact transitioned to



345 NO_x-limited regimes. Overall, Fig. 7 demonstrates that the long-term record of OMI observations can observe the impact of global
346 emissions reduction strategies on air quality and O₃ sensitivity regimes throughout the Northern Hemisphere.

347 **3.5 Impact of the COVID-lockdown on FNRs in the Northern Hemisphere**

348 The global impacts of the COVID-lockdown in 2020 on atmospheric pollution, such as the reduction of tropospheric NO₂, has
349 been well documented (e.g., Goldberg et al., 2020; He et al., 2020, Cooper et al., 2022). Here we studied, for the first time, OMI
350 derived VCD FNRs to evaluate the impact of the COVID-lockdown on summer-mean FNRs in 2020 throughout the Northern
351 Hemisphere compared to the year before (2019) and after (2021). Figure 8 shows the changes in OMI FNRs before, during, and
352 after (2019, 2020, 2021) the COVID-lockdown over the selected 46 cities discussed in this study. Out of the 46 selected cities, 32
353 of the urban regions (~70%) experienced higher FNRs in 2020 compared to 2019. On average, the cities that experienced increased
354 FNRs in 2020 had values which were ~19% higher compared to 2019. Similarly, 26 of the urban regions (~57%) experienced
355 higher FNRs in 2020 compared to 2021 and these city centers had FNR values ~18% larger. OMI also retrieved increased FNR
356 values in rural regions surrounding city centers throughout the Northern Hemisphere during the COVID-lockdown period of 2020
357 (see Fig. 8). A similar number of city's rural areas experienced increased FNRs in 2020 compared to 2019 and 2021 as what was
358 observed for urban areas. The increases in FNRs for rural regions in 2020 compared to 2019 and 2021 were 16% and 13%. The
359 OMI data evaluated here suggest that the majority of cities in the Northern Hemisphere, and surrounding rural regions, tended to
360 have O₃ production which was more sensitivity to NO_x emissions/concentrations in 2020 compared to the year before and after.
361 Cooper et al. (2022) demonstrated that in 2020 NO₂ concentrations were on average ~30% lower during COVID-lockdown periods
362 and these reductions were from decreased anthropogenic emissions and can't be explained by meteorological differences. The
363 degree of reduction in NO₂ determined in Cooper et al. (2022) agrees well with the OMI VCD FNR increases determined during
364 our study of ~20%.

365 **4. Discussing the use of OMI data to assess O₃ production sensitivity regimes**

366 The OMI satellite sensor offers a continuous data record across the globe with sufficient spatiotemporal resolution to assess
367 tropospheric O₃ production sensitivity which cannot be achieved with in situ observations. The analysis in this study demonstrated
368 that the 17-year record of OMI-retrieved HCHO and NO₂ data offered an unprecedented opportunity to assess the long-term
369 evolution of VCD, and likely surface-level, FNR values, with potential future applications in linking these ratio changes with
370 changes in surface O₃ regimes. Here we show that OMI VCD data of FNRs replicate the trends observed with surface in situ
371 information. In order to produce actual satellite-derived surface values of HCHO, NO₂, and FNRs using VCD retrievals requires
372 algorithms which largely depend on CTM-predicted vertical distributions of these trace gases (e.g. Zhu et al., 2017a; Jin et al.,
373 2017; Cooper et al., 2020). Surface-based and aircraft in situ observations are also used for this purpose; however, these
374 observations have minimal observational coverage due to being very spatiotemporally limited (e.g., Souri et al., 2023a). Using
375 model simulations or in situ data to convert satellite VCD information to surface-level HCHO, NO₂, and FNRs concentrations are
376 both inhibited by errors. In situ observations are too sparse and CTMs have system-specific errors/biases and differ largely in their
377 prediction of HCHO and NO₂ vertical distributions (Lamsal et al., 2008; Geddes et al., 2016; Souri et al., 2023b). This results in
378 large uncertainties in surface-level FNRs when convolving satellite VCDs. Our study does not address the conversion of OMI
379 VCDs to surface-level values, but clearly shows that this spaceborne sensor can capture the trends in surface-level FNRs. The
380 ability of VCD information from low earth orbit satellites to capture mid-day surface-level FNR trends might be due to studies
381 showing ratios of VCD FNRs to PBL/surface values are near unity (Jin et al., 2017; Souri et al., 2023a). However, during times
382 where HCHO and NO₂ vertical profiles in the troposphere are not similar to climatological averages, models and satellites may be



383 challenged to accurately assess conversion ratios of VCD FNRs to PBL/surface values (e.g., Souri et al., 2023b). Overall, if
384 methods are improved to reduce the uncertainty in the conversion of satellite VCD retrievals of HCHO and NO₂ to surface-level
385 concentrations, then satellite-derived surface-level FNRs will be able to be applied in higher confidence for air quality research
386 and potentially policy decisions.

387 OMI VCD FNR and NO₂ retrievals display high correlation with surface in situ data trends (see Table 1). However, this
388 satellite demonstrated less capability to replicate trends of surface-level observations of HCHO. The vertical structure of HCHO
389 can be complex which complicates the relationship between VCDs and surface-level values (Souri et al., 2023b); however, OMI
390 has also been shown to have large systematic and random biases in HCHO retrievals which drive the overall errors in OMI-derived
391 VCD FNRs (Johnson et al., 2023; Souri et al., 2023a). However, since decreasing NO₂ emissions/concentrations are the primary
392 reason for the increasing trends of FNRs at the surface, while HCHO has near-neutral trends, and OMI NO₂ VCDs have much
393 lower errors compared to HCHO (Johnson et al., 2023; Souri et al., 2023a), this study shows that OMI VCD data of indicator
394 species can still replicate surface-level trends of FNRs. In addition to retrieval errors, the coarse spatial resolution of OMI and
395 other spaceborne sensors results in representation errors when compared to point-source surface observations (Souri et al., 2022).
396 This also likely contributes to the challenge of satellite-derived HCHO, NO₂, and FNRs to replicate trends and variability
397 determined from in situ measurements located in city centers.

398 Besides the southeast US and some small areas of eastern China, OMI HCHO version 3 collection 3 data results in mostly
399 positive trends between 2005-2021. A portion of this positive trend could be due to the OMI instrument drift which has been
400 identified in past studies (e.g., Marais et al., 2012; Zhu et al., 2016, 2017b). Currently, there is an OMI HCHO version 3 collection
401 4 product in development using the SAO algorithm; however, has yet to be published and therefore could not be applied in this
402 study. A major difference between the collection 3 and 4 data products is how level 1b (L1b) data is produced as described in
403 Kleipool et al. (2022). Furthermore, changes in molecular absorption cross-sections and input parameters for SCD calculations,
404 AMF calculations, and latitudinal bias corrections are applied in collection 4 OMI HCHO data. Preliminary analysis of the
405 differences in OMI VCD HCHO using the collection 3 and 4 data demonstrates changes in the magnitudes and trends of this
406 species (personal communication with the SAO OMI HCHO algorithm team). These differences could have an impact on the
407 analysis of trends in global FNRs such as that conducted in this study. Once the OMI HCHO version 3 collection 4 product becomes
408 available to the public the analysis in this study should be redone with the updated HCHO data. Overall, we don't expect that the
409 results in FNR trends will be impacted much due to observed trends in OMI VCD and surface-level NO₂ being much larger than
410 that in HCHO (see Sect. 3.2).

411 Due to the inadequacy of our current quantitative understanding of exact threshold FNR values marking the O₃
412 photochemical regime transitions (e.g., Schroeder et al., 2017), this study avoided explicitly linking OMI FNRs with exact chemical
413 regimes. An accurate diagnosis of surface O₃ sensitivity requires more in-depth analysis of satellite FNRs at a higher spatiotemporal
414 resolution, and accurately relating these FNRs to O₃ regimes by estimating the threshold ratio values applicable to specific regions
415 and time periods. Global CTM simulations (Jin et al., 2017), photochemical box modeling utilizing measurement data from
416 airborne field campaigns (Schroeder et al., 2017; Souri et al., 2020), and observation-based methods linking ratio values with
417 surface O₃ concentrations (Jin et al., 2020; Wang et al., 2021) could lead to the derivation of more accurate regime threshold ratio
418 values. Nevertheless, the OMI-derived VCD FNR values investigated in this study revealed many aspects of O₃ sensitivity to NO_x
419 versus VOCs. In general, OMI-derived summer FNR values indicated radical limited regimes within many cities in the Northern
420 Hemisphere (FNRs < 2) and NO_x-limited regimes over the rural regions around those cities (FNRs > 3). The analysis of multi-year
421 summer mean OMI HCHO and NO₂ values revealed a positive trend in FNRs indicating a transition from radical-limited to NO_x-
422 limited regimes, especially during more recent years. The positive trend in OMI FNRs over most cities are mainly due to decreases



423 in NO₂ resulting from the decrease in anthropogenic NO_x emissions and mixed-variations in biogenic VOC sources. This study
424 evaluated FNR trends for 46 large Northern Hemisphere cities which expands on other recent studies which evaluated O₃
425 production sensitivity regimes around smaller numbers of cities (e.g., Jin et al., 2017). Due to the majority of highly-populated
426 Northern Hemisphere cities, outside of the Tropics, residing in developed nations, the increasing trend in FNRs due to
427 anthropogenic emissions reductions holds true for the vast majority of the 46 cities studied here.

428 In the earliest years of studying satellite-derived FNRs it was hoped this data source could potentially be used for policy
429 decisions and developing emission control strategies (Martin et al., 2004). However, more recent studies starting with Duncan et
430 al. (2010) suggested that satellite retrievals may have errors too large for applying FNRs for air quality regulations. Furthermore,
431 satellite data typically has to be temporally averaged to reduce noise in the retrievals which may mask out important O₃ exceedance
432 events and the indicator species characteristics on these days (Schroeder et al., 2017). The recent study by Souri et al. (2023a)
433 compiled a comprehensive error budget for using satellite retrievals to assess surface-level FNRs. This study showed that total
434 relative error in satellite FNRs over large cities tend to be ~50% whereas over rural regions there are much larger errors (>100%).
435 The majority of this error comes from noise in satellite retrievals (40%-90%), especially from HCHO retrievals, and the rest of
436 this error is associated with the ability of indicator species to accurately describe complex O₃ chemistry (~20%), VCD to surface
437 translation (~19%), and spatial representation (~13%). These total relative errors are likely too large to apply satellite FNRs for air
438 quality regulation purposes; however, still provide a useful scientific research product for investigating long-term, and short-term
439 events (e.g., meteorological variations, droughts/floods, wildfires, socioeconomic events, etc.), impacts of emissions on O₃
440 production sensitivity regimes.

441 **4 Conclusions**

442 This study applied the 17-year data record of OMI satellite sensor's summer mean VCD HCHO, NO₂, and FNRs between 2005
443 and 2021 over the Northern Hemisphere to understand the long-term evolution of O₃ photochemical regimes. This expands the
444 global OMI record of VCD FNRs out to 2021 further than previous studies (e.g., Jin et al., 2020). The long-term trends for 46
445 highly populated cities in the Northern Hemisphere agree with past work which have shown that FNRs are primarily increasing
446 due to reductions in emissions/concentrations of NO_x (Duncan et al., 2010; Jin et al., 2017, 2020). OMI VCD NO₂ data are
447 decreasing in most urban regions of the Northern Hemisphere, while HCHO data is near-neutral or slightly increasing, resulting in
448 the increasing FNR trends. The extension of OMI FNR data out to 2021 suggests a continuing trend towards more NO_x-limited O₃
449 production sensitivity regimes within and around cities throughout the Northern Hemisphere.

450 Another unique finding in our study is the extension of OMI FNR data out to 2021 covering the impact of the COVID-
451 19 lockdown of 2020. Out of the 46 selected cities, ~70% of urban regions experienced higher FNRs in 2020 compared to 2019
452 and ~57% had higher FNRs in 2020 compared to 2021. OMI FNRs were 18%-19% higher in 2020 compared to the year before
453 and after the COVID-lockdown in 2020. We studied summer-mean FNRs in this study; however, COVID-lockdown restrictions
454 were largest in the spring of 2020, thus the full impact of COVID-lockdown restrictions on VCD FNRs was likely larger than that
455 experienced in the summer. A similar percentage of rural areas around the 46 selected cities experience higher FNRs in 2020
456 compared to 2019 and 2021; however, the increases in FNRs were smaller (13%-16%) compared to urban areas. The OMI data
457 evaluated here suggests that the majority of cities in the Northern Hemisphere, and surrounding rural regions, tended to have O₃
458 production which was more sensitive to NO_x emissions/concentrations in 2020 compared to the year before and after.

459 Past studies have shown that mid-day FNR VCDs are similar to those observed at the surface (Jin et al., 2017; Souri et
460 al., 2023a). However, during times where HCHO and NO₂ vertical profiles in the troposphere are complex, models and satellites
461 may be challenged to accurately assess conversion ratios of VCD FNRs to PBL/surface values (e.g., Souri et al., 2023b). This



462 study shows that on average the long-term trends of OMI VCD FNRs agree well with in observations at the surface in cities
463 distributed around the US, suggesting that this satellite is capable to assess the long-term trends of surface-level O₃ production
464 sensitivity regimes. However, the magnitudes of both indicator species calculated with satellite VCDs using scaling factors derived
465 with CTMs and/or in situ observations are highly uncertain. Both OMI VCD and surface in situ data of HCHO, NO₂, and FNRs
466 emphasize that the increasing trend in FNRs is driven by reduced emissions/concentrations of NO₂ while HCHO has a near-neutral
467 trend. While OMI VCD HCHO trends and variability do not agree well with surface in situ observations; OMI does replicate the
468 strong decreasing trend of NO₂ observed at the surface resulting in the agreement between OMI and surface data of FNR trends.

469 Higher spatiotemporal retrievals from newer low earth orbit (e.g., TROPOspheric Monitoring Instrument [TROPOMI])
470 and geostationary (e.g., Tropospheric Emissions: Monitoring of Pollution [TEMPO], Geostationary Environment Monitoring
471 Spectrometer [GEMS]) satellite sensors provide more insight into the short-term (daily, diurnal) recent (2017-present) evolution
472 of O₃ photochemical regimes. Compared to OMI, TROPOMI was shown to retrieve VCD FNR values with more accuracy and
473 better precision compared to OMI observations primarily due to improvements in HCHO product performance (e.g., Johnson et
474 al., 2023). Johnson et al. (2023) demonstrated that TROPOMI can retrieve spatiotemporal HCHO variability with uncertainties
475 low enough to capture FNR variability on a daily basis, while OMI was not. Future improvements in satellite HCHO retrievals
476 will allow for more accurate retrievals of FNRs on a daily- to monthly-scale. TEMPO and GEMS provide HCHO and NO₂ VCD
477 information at 1- to 3-hour temporal resolution which will allow for the assessment of diurnal FNR variability on a regional scale.
478 This has not yet been possible as TEMPO and GEMS are the first UV/VIS spectrometers on geostationary platforms with spatial
479 resolution high enough to retrieve air quality relevant HCHO and NO₂ VCD data. As OMI is set to be decommissioned in the
480 coming years, it is critical to merge TROPOMI HCHO and NO₂ VCD data with OMI in order to continue the long-term data set
481 from 2005-present. Furthermore, combining retrieved information from geostationary satellites with once-a-day low earth orbit
482 data will provide a vast wealth of information about global daily to hourly variability in FNRs.

483 While recent studies have shown that OMI FNR retrieval errors are likely too large to apply in air quality regulation and
484 for deriving emission control strategies to reduce surface-level O₃ concentrations, this long-term satellite product provides a useful
485 scientific research product for investigating atmospheric O₃ chemistry and investigating qualitative impacts of emission changes
486 on O₃ production sensitivity regimes. This is especially true for regions of the globe outside of the US and Europe that have limited
487 long-term surface in situ observation networks able to measure HCHO and NO₂ concentrations. Improvements in HCHO and NO₂
488 VCD retrieval algorithms and methods to derive VCD to surface/PBL conversion factors for these indicator species would greatly
489 improve the ability to apply OMI and other satellite products to study surface air quality. Data assimilation and inverse models
490 have been combined with satellite retrievals of HCHO and NO₂ data to constrain predictions of NO_x and VOC emissions and
491 resulting O₃ chemistry (e.g., Souri et al., 2020). These satellite data-constrained models can then be used to assess trends and
492 variability in FNRs, indicator species emissions, and O₃ photochemistry regimes. These improvements in satellite retrieval
493 algorithms, CTMs, data assimilation and inverse modeling techniques, along with studies to better define the actual O₃ production
494 sensitivity regime thresholds, will allow for a more confident investigation of long-term air quality and the impacts of NO_x and
495 VOC emission changes on O₃ production sensitivity.

496 *Code and Data Availability.* The OMI HCHO L3 data used in this paper is publicly available at
497 https://acdisc.gesdisc.eosdis.nasa.gov/data/Aura_OMI_Level3/OMHCHOd.003/ (last access: 24 October 2021). The OMI NO₂
498 High Resolution L3 data is also available at a public data repository:



499 https://avdc.gsfc.nasa.gov/pub/data/satellite/Aura/OMI/V03/L3/OMNO2d_HR/OMNO2d_HRD/ (last access: 3 December 2021).

500 The CEDS emission inventory used in this work is also publicly available (<https://data.pnnl.gov/group/nodes/dataset/13488>) (last
501 access: July 22, 2023). EPA AQS data of HCHO and NO₂ can be downloaded from: [https://www.epa.gov/outdoor-air-quality-](https://www.epa.gov/outdoor-air-quality-data/download-daily-data)
502 [data/download-daily-data](https://www.epa.gov/outdoor-air-quality-data/download-daily-data) (last access: August 3, 2023).

503 *Supplement.* The supplement related to this article is available.

504 *Author Contributions.* MJ and SP obtained the funding for this project. MJ, SP, and RK were fundamental in developing the
505 investigation strategy of this study. SJ, SP, SM, S M-H, and YS conducted the analysis which produce the results presented in this
506 manuscript. Finally, MJ and SP were the primary authors which wrote the text of the manuscript.

507 *Competing interests.* The authors declare that they have no conflict of interest.

508 *Acknowledgements.* Computational resources were provided by the NASA High-End Computing Program through the NASA
509 Advanced Supercomputing Division at NASA Ames Research Center. We acknowledge the United States Environmental
510 Protection Agency for the free availability of in situ data. The views, opinions and findings of this paper are those of the authors
511 and should not be construed as an official NASA or United States Government position, policy, or decision.

512 *Financial support.* The MJ, SP, SM, RK, S M-H, and YS acknowledge funding support from the NASA Earth Science Division's
513 Aura Science Team (NNH19ZDA001N-AURAST) as part of the Upper Atmosphere Research Program (UARP). A part of this
514 material is based upon work supported by the NSF National Center for Atmospheric Research, which is a major facility sponsored
515 by the U.S. National Science Foundation under Cooperative Agreement No. 1852977.

516



517 **References**

- 518 Acdan, J. J. M., Pierce, R. B., Dickens, A. F., Adelman, Z., and Nergui, T.: Examining TROPOMI formaldehyde to nitrogen
519 dioxide ratios in the Lake Michigan region: implications for ozone exceedances, *Atmos. Chem. Phys.*, 23, 7867–7885,
520 <https://doi.org/10.5194/acp-23-7867-2023>, 2023.
- 521 Boersma, K. F., Eskes, H. J., Dirksen, R. J., van der A, R. J., Veefkind, J. P., Stammes, P., Huijnen, V., Kleipool, Q. L., Sneep,
522 M., Claas, J., Leitão, J., Richter, A., Zhou, Y., and Brunner, D.: An improved tropospheric NO₂ column retrieval algorithm
523 for the Ozone Monitoring Instrument, *Atmos. Meas. Tech.*, 4, 1905–1928, <https://doi.org/10.5194/amt-4-1905-2011>, 2011.
- 524 Boys, B., Martin, R., van Donkelaar, A., MacDonell, R., Hsu, C., Cooper, M., Yantosca, R., Lu, Z., Streets, D. G., Zhang, Q., and
525 Wang, S.: Fifteen-year global time series of satellite-derived fine particulate matter, *Environ. Sci. Technol.*, 48, 11109–11118,
526 2014.
- 527 Bucsela, E. J., Krotkov, N. A., Celarier, E. A., Lamsal, L. N., Swartz, W. H., Bhartia, P. K., Boersma, K. F., Veefkind, J. P.,
528 Gleason, J. F., and Pickering, K. E.: A new stratospheric and tropospheric NO₂ retrieval algorithm for nadir-viewing satellite
529 instruments: applications to OMI, *Atmos. Meas. Tech.*, 6, 2607–2626, <https://doi.org/10.5194/amt-6-2607-2013>, 2013.
- 530 Burrows, J. P., Weber, M., Buchwitz, M., Rozanov, V., Ladstätter-Weissenmayer, A., Richter, A., DeBeek, R., Hoogen, R.,
531 Bramstedt, K., Eichmann, K.-U., Eisingera, M., and Pernerb, D.: The global ozone monitoring experiment (GOME): Mission
532 concept and first scientific results, *J. Atmos. Sci.*, 56, 151–175, 1999.
- 533 Camalier, L., Cox, W., and Dolwick, P.: The effects of meteorology on ozone in urban areas and their use in assessing ozone
534 trends, *Atmos. Environ.*, 41, 7127–7137, doi: 10.1016/j.atmosenv.2007.04.061, 2007.
- 535 Chance, K. V. and Spurr, R. J. D.: Ring effect studies: Rayleigh scattering, including molecular parameters for rotational Raman
536 scattering, and the Fraunhofer spectrum, *Appl. Optics*, 36, 5224–5230, doi:10.1364/AO.36.005224, 1997.
- 537 Chance, K.: Analysis of BrO measurements from the Global Ozone Monitoring Experiment, *Geophys. Res. Lett.*, 25, 3335–3338,
538 <https://doi.org/10.1029/98GL52359>, 1998.
- 539 Chang, C. -Y., Faust, E., Hou, X., Lee, P., Kim, H. C., Hedquist, B. C., and Liao, K. -J.: Investigating ambient ozone formation
540 regimes in neighboring cities of shale plays in the northeast United States using photochemical modeling and satellite
541 retrievals, *Atmos. Environ.*, 142, 152–170. doi:10.1016/j.atmosenv.2016.06.058, 2016.
- 542 Choi, Y. and Souri, A.: Chemical condition and surface ozone in large cities of Texas during the last decade: observational evidence
543 from OMI, CAMS, and Model Analysis, *Remote Sens. Environ.*, 168, 90–101, <https://doi.org/10.1016/j.rse.2015.06.026>,
544 2015.
- 545 Choi, Y., Kim, H., Tong, D., and Lee, P.: Summertime weekly cycles of observed and modeled NO_x and O₃ concentrations as a
546 function of satellite-derived ozone production sensitivity and land use types over the Continental United States, *Atmos. Chem.*
547 *Phys.*, 12, 6291–6307, doi:10.5194/acp-12-6291-2012, 2012.
- 548 Cooper, M. J., Martin, R. V., McLinden, C. A., and Brook, J. R.: Inferring ground-level nitrogen dioxide concentrations at fine
549 spatial resolution applied to the TROPOMI satellite instrument, *Environ. Res. Lett.*, 15, 104013, <https://doi.org/10.1088/1748-9326/aba3a5>, 2020.
- 551 Cooper, M. J., Martin, R. V., Hammer, M. S., Levelt, P. F., Veefkind, P., Lamsal, L. N., Krotkov, N. A., Brook, J. R., and
552 McLinden, C. A.: Global fine-scale changes in ambient NO₂ during COVID-19 lockdowns, *Nature*, 601, 380–387,
553 [10.1038/s41586-021-04229-0](https://doi.org/10.1038/s41586-021-04229-0), 2022.



- 554 Dave, J. V.: Meaning of successive iteration of the auxiliary equation in the theory of radiative transfer, *Astrophys. J.*, 140, 1292–
555 1303, 1964.
- 556 De Smedt, I., Stavrou, T., Hendrick, F., Danckaert, T., Vlemmix, T., Pinardi, G., Theys, N., Lerot, C., Gielen, C., Vigouroux,
557 C., Hermans, C., Fayt, C., Veefkind, P., Müller, J.-F., and Van Roozendael, M.: Diurnal, seasonal and long-term variations of
558 global formaldehyde columns inferred from combined OMI and GOME-2 observations, *Atmos. Chem. Phys.*, 15, 12519–
559 12545, <https://doi.org/10.5194/acp-15-12519-2015>, 2015.
- 560 De Smedt, I., Theys, N., Yu, H., Danckaert, T., Lerot, C., Compernelle, S., Van Roozendael, M., Richter, A., Hilboll, A., Peters,
561 E., Pedernana, M., Loyola, D., Beirle, S., Wagner, T., Eskes, H., van Geffen, J., Boersma, K. F., and Veefkind, P.: Algorithm
562 theoretical baseline for formaldehyde retrievals from S5P TROPOMI and from the QA4ECV project, *Atmos. Meas. Tech.*,
563 11, 2395–2426, <https://doi.org/10.5194/amt-11-2395-2018>, 2018.
- 564 Demuzere, M., He, C., Martilli, A., Zonato, A.: Technical documentation for the hybrid 100-m global land cover dataset with Local
565 Climate Zones for WRF. <https://doi.org/10.5281/zenodo.7670791>, 2023.
- 566 Dobber, M., Kleipool, Q., Dirksen, R., Levelt, P., Jaross, G., Taylor, S., Kelly, T., and Flynn, L.: Validation of ozone monitoring
567 instrument level-1b data products, *J. Geophys. Res.*, 113, D15S06, <https://doi.org/10.1029/2007JD008665>, 2008.
- 568 Duncan, B., Yoshida, Y., Olson, J., Sillman, S., Martin, R., Lamsal, L., Hu, Y., Pickering, K., Retscher, D., Allen, D., and Crawford,
569 J.: Application of OMI observations to a space-based indicator of NO_x and VOC controls on surface ozone formation, *Atmos.*
570 *Environ.*, 44, 2213–2223, <https://doi.org/10.1016/j.atmosenv.2010.03.010>, 2010.
- 571 Fan, C., Li, Z., Li, Y., Dong, J., van der A, R., and de Leeuw, G.: Variability of NO₂ concentrations over China and effect on air
572 quality derived from satellite and ground-based observations, *Atmos. Chem. Phys.*, 21, 7723–7748,
573 <https://doi.org/10.5194/acp-21-7723-2021>, 2021.
- 574 Geddes, J. A., Martin, R. V., Boys, B. L., and van Donkelaar, A.: Long term trends worldwide in ambient NO₂ concentrations
575 inferred from satellite observations, *Environ. Health Perspect.*, doi:10.1289/ehp.1409567, 2016.
- 576 GBD 2019 Risk Factor Collaborators: Global burden of 87 risk factors in 204 countries and territories, 1990–2019: a systematic
577 analysis for the Global Burden of Disease Study 2019, *The Lancet*, 396, 1223–1249, [https://doi.org/10.1016/s0140-6736\(20\)30752-2](https://doi.org/10.1016/s0140-6736(20)30752-2), 2020.
- 579 Goldberg, D. L., Anenberg, S. C., Griffin, D., McLinden, C. A., Lu, Z., and Streets, D. G.: Disentangling the Impact of the COVID-
580 19 Lockdowns on Urban NO₂ From Natural Variability, *Geophys. Res. Lett.*, 47, e2020GL089269,
581 <https://doi.org/10.1029/2020GL089269>, 2020.
- 582 González Abad, G., Liu, X., Chance, K., Wang, H., Kurosu, T. P., and Suleiman, R.: Updated Smithsonian Astrophysical
583 Observatory Ozone Monitoring Instrument (SAO OMI) formaldehyde retrieval, *Atmos. Meas. Tech.*, 8, 19–32,
584 doi:10.5194/amt-8-19-2015, 2015.
- 585 González Abad, G., Souri, A. H., Bak, J., Chance, K., Flynn, L. E., Krotkov, N. A., Lamsal, L., Li, C., Liu, X., Miller, C. C.,
586 Nowlan, C. R., Suleiman, R., and Wang, H.: Five decades observing Earth's atmospheric trace gases using ultraviolet and
587 visible backscatter solar radiation from space, *J. Quant. Spectrosc. Ra.*, 238, 106478,
588 <https://doi.org/10.1016/j.jqsrt.2019.04.030>, 2019.
- 589 He, G., Pan, Y. and Tanaka, T.: The short-term impacts of COVID-19 lockdown on urban air pollution in China, *Nature*
590 *Sustainability*, 3(12), 1005–1011, <https://doi.org/10.1038/s41893-020-0581-y>, 2020.



- 591 Hilboll, A., Richter, A., and Burrows, J. P.: Long-term changes of tropospheric NO₂ over megacities derived from multiple satellite
592 instruments, *Atmos. Chem. Phys.*, 13, 4145–4169, <https://doi.org/10.5194/acp-13-4145-2013>, 2013.
- 593 Itahashi, S., Irie, H., Shimadera, H., and Chatani, S.: Fifteen-Year Trends (2005–2019) in the Satellite-Derived Ozone-Sensitive
594 Regime in East Asia: A Gradual Shift from VOC-Sensitive to NO_x-Sensitive, *Remote Sens.*, 14, 4512,
595 <https://doi.org/10.3390/rs14184512>, 2022.
- 596 Jacob, D. J., Horowitz, L. W., Munger, J. W., Heikes, B. G., Dickerson, R. R., Artz, R. S., and Keene, W. C.: Seasonal transition
597 from NO_x- to hydrocarbon-limited conditions for ozone production over the eastern United States in September, *J. Geophys.*
598 *Res.-Atmos.*, 100, 9315–9324, <https://doi.org/10.1029/94JD03125>, 1995.
- 599 Jin, X., and Holloway, T.: Spatial and temporal variability of ozone sensitivity over China observed from the Ozone Monitoring
600 Instrument, *J. Geophys. Res. Atmos.*, 120, 7229–7246, doi:10.1002/2015JD023250, 2015.
- 601 Jin, X., Fiore, A. M., Murray, L. T., Valin, L. C., Lamsal, L. N., Duncan, B., Boersma, K. F., De Smedt, I., Abad, G. G., Chance,
602 K., and Tonnesen, G. S.: Evaluating a Space-Based Indicator of Surface Ozone-NO_x-VOC Sensitivity Over Midlatitude
603 Source Regions and Application to Decadal Trends, *J. Geophys. Res.-Atmos.*, 122, 10439–10461,
604 <https://doi.org/10.1002/2017JD026720>, 2017.
- 605 Jin, X., Fiore, A. M., and Geigert, M.: Using satellite observed formaldehyde (HCHO) and nitrogen dioxide (NO₂) as an indicator
606 of ozone sensitivity in a SIP, HAQAST Tech. Guid. Doc. No. 1, doi:10.7916/D8M34C7V, 2018.
- 607 Jin, X., Fiore, A., Boersma, K. F., De Smedt, I., and Valin, L.: Inferring Changes in Summertime Surface Ozone–NO_x–VOC
608 Chemistry over U.S. Urban Areas from Two Decades of Satellite and Ground-Based Observations, *Environ. Sci. Technol.*,
609 54, 6518–6529, <https://doi.org/10.1021/acs.est.9b07785>, 2020.
- 610 Johnson, M. S., Souri, A. H., Philip, S., Kumar, R., Naeger, A., Geddes, J., Judd, L., Janz, S., Chong, H., and Sullivan, J.: Satellite
611 remote-sensing capability to assess tropospheric-column ratios of formaldehyde and nitrogen dioxide: case study during the
612 Long Island Sound Tropospheric Ozone Study 2018 (LISTOS 2018) field campaign, *Atmos. Meas. Tech.*, 16, 2431–2454,
613 <https://doi.org/10.5194/amt-16-2431-2023>, 2023.
- 614 Kharol, S. K., Martin, R. V., Philip, S., Boys, B., Lamsal, L. N., Jerrett, M., Brauer, M., Crouse, D. L., McLinden, C., and Burnett,
615 R. T.: Assessment of the magnitude and recent trends in satellite-derived ground-level nitrogen dioxide over North America,
616 *Atmos. Environ.*, 118, 236–245, <https://doi.org/10.1016/j.atmosenv.2015.08.011>, 2015.
- 617 Kleinman, L. I.: Low and high NO_x tropospheric photochemistry, *J. Geophys. Res.*, 99, 16831–16838, 1994.
- 618 Kleinman, L. I., Daum, P. H., Lee, Y. N., Nunnermacker, L. J., Springston, S. R., Weinstein-Lloyd, J., and Rudolph, J.: A
619 comparative study of ozone production in five US metropolitan areas, *J. Geophys. Res.-Atmos.*, 110, D02301,
620 doi:10.1029/2004JD005096, 2005.
- 621 Kleipool, Q., Rozemeijer, N., van Hoek, M., Leloux, J., Loots, E., Ludewig, A., van der Plas, E., Adrichem, D., Harel, R., Spronk,
622 S., ter Linden, M., Jaross, G., Haffner, D., Veeffkind, P., and Levelt, P. F.: Ozone Monitoring Instrument (OMI) collection 4:
623 establishing a 17-year-long series of detrended level-1b data, *Atmos. Meas. Tech.*, 15, 3527–3553,
624 <https://doi.org/10.5194/amt-15-3527-2022>, 2022.
- 625 Krotkov, N. A., McLinden, C. A., Li, C., Lamsal, L. N., Celarier, E. A., Marchenko, S. V., Swartz, W. H., Bucsela, E. J., Joiner,
626 J., Duncan, B. N., Boersma, K. F., Veeffkind, J. P., Levelt, P. F., Fioletov, V. E., Dickerson, R. R., He, H., Lu, Z., and Streets,
627 D. G.: Aura OMI observations of regional SO₂ and NO₂ pollution changes from 2005 to 2015, *Atmos. Chem. Phys.*, 16,
628 4605–4629, <https://doi.org/10.5194/acp-16-4605-2016>, 2016.



- 629 Krotkov, N. A., Lamsal, L. N., Celarier, E. A., Swartz, W. H., Marchenko, S. V., Bucsela, E. J., Chan, K. L., Wenig, M., and Zara,
630 M.: The version 3 OMI NO₂ standard product, *Atmos. Meas. Tech.*, 10, 3133–3149, [https://doi.org/10.5194/amt-10-3133-](https://doi.org/10.5194/amt-10-3133-2017)
631 2017, 2017.
- 632 Lamsal, L. N., Martin, R. V., Steinbacher, M., Celarier, E. A., Bucsela, E., Dunlea, E. J., and Pinto, J.: Ground level nitrogen
633 dioxide concentrations inferred from the satellite-borne Ozone Monitoring Instrument, *J. Geophys. Res.*, 113, D16308,
634 <https://doi.org/10.1029/2007JD009235>, 2008.
- 635 Lamsal, L. N., Martin, R. V., van Donkelaar, A., Celarier, E. A., Bucsela, E. J., Boersma, K. F., Dirksen, R., Luo, C., and Wang,
636 Y.: Indirect validation of tropospheric nitrogen dioxide retrieved from the OMI satellite instrument: Insight into the seasonal
637 variation of nitrogen oxides at northern midlatitudes, *J. Geophys. Res.*, 115, D05302, <https://doi.org/10.1029/2009JD013351>,
638 2010.
- 639 Lamsal, L. N., Duncan, B. N., Yoshida, Y., Krotkov, N. A., Pickering, K. E., Streets, D. G., and Lu, Z.: U.S. NO₂ trends (2005–
640 2013): EPA Air Quality System (AQS) data versus improved observations from the Ozone Monitoring Instrument (OMI),
641 *Atmos. Environ.*, 110, 130–143, doi:10.1016/j.atmosenv.2015.03.055, 2015.
- 642 Levelt, P. F., Hilsenrath, E., Leppelmeier, G. W., Oord, G. H. J. Van Den, Bhartia, P. K., Tamminen, J., De Haan, J. F., and
643 Veefkind, J. P.: Science Objectives of the Ozone Monitoring Instrument, *IEEE T. Geosci. Remote Sens.*, 44, 1199–1208,
644 2006.
- 645 Levelt, P. F., Joiner, J., Tamminen, J., Veefkind, J. P., Bhartia, P. K., Stein Zweers, D. C., Duncan, B. N., Streets, D. G., Eskes,
646 H., van der A, R., McLinden, C., Fioletov, V., Carn, S., de Laat, J., DeLand, M., Marchenko, S., McPeters, R., Ziemke, J., Fu,
647 D., Liu, X., Pickering, K., Apituley, A., González Abad, G., Arola, A., Boersma, F., Chan Miller, C., Chance, K., de Graaf,
648 M., Hakkarainen, J., Hassinen, S., Ialongo, I., Kleipool, Q., Krotkov, N., Li, C., Lamsal, L., Newman, P., Nowlan, C.,
649 Suleiman, R., Tilstra, L. G., Torres, O., Wang, H., and Wargan, K.: The Ozone Monitoring Instrument: overview of 14 years
650 in space, *Atmos. Chem. Phys.*, 18, 5699–5745, <https://doi.org/10.5194/acp-18-5699-2018>, 2018.
- 651 Li, Y., Lau, A. K. H., Fung, J. C. H., Zheng, J. Y., Zhong, L. J., and Louie, P. K. K.: Ozone source apportionment (OSAT) to
652 differentiate local regional and super-regional source contributions in the Pearl River Delta region, China, *J. Geophys. Res.-*
653 *Atmos.*, 117, 1–18, <https://doi.org/10.1029/2011JD017340>, 2012.
- 654 Mahajan, A. S., De Smedt, I., Biswas, M. S., Ghude, S., Fadnavis, S., Roy, C., and van Roozendaal, M.: Inter-annual variations in
655 satellite observations of nitrogen dioxide and formaldehyde over India, *Atmos. Environ.*, 116, 194–201,
656 <https://doi.org/10.1016/j.atmosenv.2015.06.004>, 2015.
- 657 Marais, E. A., Jacob, D. J., Kurosu, T. P., Chance, K., Murphy, J. G., Reeves, C., Mills, G., Casadio, S., Millet, D. B., Barkley, M.
658 P., Paulot, F., and Mao, J.: Isoprene emissions in Africa inferred from OMI observations of formaldehyde columns, *Atmos.*
659 *Chem. Phys.*, 12, 6219–6235, <https://doi.org/10.5194/acp-12-6219-2012>, 2012.
- 660 Marchenko, S., Krotkov, N., Lamsal, L., Celarier, E., Swartz, W., and Bucsela, E.: Revising the slant column density retrieval of
661 nitrogen dioxide observed by the Ozone Monitoring Instrument, *J. Geophys. Res.*, 120, 5670–5692,
662 <https://doi.org/10.1002/2014JD022913>, 2015.
- 663 Martin, R. V., Fiore, A. M., and Van Donkelaar, A.: Space-based diagnosis of surface ozone sensitivity to anthropogenic
664 emissions, *Geophys. Res. Lett.*, 31, L06120. doi:10.1029/2004GL019416, 2004.
- 665 McDuffie, E. E., Smith, S. J., O'Rourke, P., Tibrewal, K., Venkataraman, C., Marais, E. A., Zheng, B., Crippa, M., Brauer, M.,
666 and Martin, R. V.: A global anthropogenic emission inventory of atmospheric pollutants from sector- and fuel-specific sources



- 667 (1970–2017): an application of the Community Emissions Data System (CEDS), *Earth Syst. Sci. Data*, 12, 3413–3442,
668 <https://doi.org/10.5194/essd-12-3413-2020>, 2020.
- 669 Milford, J. B., Gao, D. F., Sillman, S., Blossey, P., and Russell, A. G.: Total reactive nitrogen (NO_y) as an indicator of the
670 sensitivity of ozone to reductions in hydrocarbon and NO_x emissions, *J. Geophys. Res.-Atmos.*, 99, 3533–3542,
671 <https://doi.org/10.1029/93jd03224>, 1994.
- 672 Millet, D. B., Jacob, D. J., Boersma, K. F., Fu, T.-M., Kurosu, T. P., Chance, K., Heald, C. L., and Guenther, A.: Spatial distribution
673 of isoprene emissions from North America derived from formaldehyde column measurements by the OMI satellite sensor, *J.*
674 *Geophys. Res.*, 113, D02307, <https://doi.org/10.1029/2007JD008950>, 2008.
- 675 Monks, P. S., Archibald, A. T., Colette, A., Cooper, O., Coyle, M., Derwent, R., Fowler, D., Granier, C., Law, K. S., Mills, G. E.,
676 Stevenson, D. S., Tarasova, O., Thouret, V., von Schneidemesser, E., Sommariva, R., Wild, O., and Williams, M. L.:
677 Tropospheric ozone and its precursors from the urban to the global scale from air quality to short-lived climate forcer, *Atmos.*
678 *Chem. Phys.*, 15, 8889–8973, <https://doi.org/10.5194/acp-15-8889-2015>, 2015.
- 679 Palmer, P. I., Jacob, D. J., Chance, K., Martin, R. V., Spurr, R. J. D., Kurosu, T. P., Bey, I., Yantosca, R., Fiore, A., and Li, Q.:
680 Air mass factor formulation for spectroscopic measurements from satellites: Application to formaldehyde retrievals from the
681 Global Ozone Monitoring Experiment, *J. Geophys. Res.-Atmos.*, 106, 14539–14550, <https://doi.org/10.1029/2000JD900772>,
682 2001.
- 683 Philip, S., Martin, R. V., van Donkelaar, A., Lo, J. W., Wang, Y., Chen, D., Zhang, L., Kasibhatla, P. S., Wang, S. W., Zhang, Q.,
684 Lu, Z., Streets, D. G., Bittman, S., and Macdonald, D. J.: Global chemical composition of ambient fine particulate matter for
685 exposure assessment, *Environ. Sci. Technol.*, 48, 13060–13068, doi:10.1021/es502965b, 2014.
- 686 Schenkeveld, V. M. E., Jaross, G., Marchenko, S., Haffner, D., Kleipool, Q. L., Rozemeijer, N. C., Veeffkind, J. P., and Levelt, P.
687 F.: In-flight performance of the Ozone Monitoring Instrument, *Atmos. Meas. Tech.*, 10, 1957–1986,
688 <https://doi.org/10.5194/amt-10-1957-2017>, 2017.
- 689 Schoeberl, M. R., Douglass, A. R., Hilsenrath, E., Bhartia, P. K., Beer, R., Waters, J. W., Gunson, M. R., Froidevaux, L., Gille, J.
690 C., Barnett, J. J., Levelt, P. F., and DeCola, P.: Overview of the EOS aura mission, *IEEE T. Geosci. Remote Sens.*, 44, 1066–
691 1072, doi:10.1109/TGRS.2005.861950, 2006.
- 692 Schroeder, J. R., Crawford, J. H., Fried, A., Walega, J., Weinheimer, A., Wisthaler, A., Müller, M., Mikoviny, T., Chen, G., Shook,
693 M., Blake, D. R., and Tonnesen, G. S.: New insights into the column CH₂ONO₂ ratio as an indicator of near-surface ozone
694 sensitivity, *J. Geophys. Res.-Atmos.*, 122, 8885–8907, <https://doi.org/10.1002/2017JD026781>, 2017.
- 695 Seinfeld, J. H. and Pandis, S. N.: *Atmospheric Chemistry and Physics: From Air Pollution to Climate Change*, John Wiley and
696 Sons, Hoboken, ISBN: 978-1-118-94740-1, 2016.
- 697 Shen, L., Jacob, D. J., Liu, X., Huang, G., Li, K., Liao, H., and Wang, T.: An evaluation of the ability of the Ozone Monitoring
698 Instrument (OMI) to observe boundary layer ozone pollution across China: application to 2005–2017 ozone trends, *Atmos.*
699 *Chem. Phys.*, 19, 6551–6560, <https://doi.org/10.5194/acp-19-6551-2019>, 2019.
- 700 Sillman, S.: The use of NO_y, H₂O₂, and HNO₃ as indicators for O₃-NO_x-hydrocarbon sensitivity in urban locations, *J. Geophys.*
701 *Res. Atmos.*, 100, 14175–14188, doi:10.1029/94JD02953, 1995.
- 702 Sillman, S.: The relation between ozone, NO_x, and hydrocarbons in urban and polluted rural environments, *Atmos. Environ.*, 33,
703 1821–1845, 1999.



- 704 Sillman, S., Logan, J. A., and Wofsy, S. C.: The sensitivity of ozone to nitrogen oxides and hydrocarbons in regional ozone
705 episodes, *J. Geophys. Res.*, 95, 1837-1851, doi: 10.1029/JD095iD02p01837, 1990.
- 706 Souri, A. H., Choi, Y., Jeon, W., Woo, J. -H., Zhang, Q., and Kurokawa J.-i.: Remote sensing evidence of decadal changes in
707 major tropospheric ozone precursors over East Asia, *J. Geophys. Res. Atmos.*, 122, 2474-2492, doi:10.1002/2016JD025663,
708 2017.
- 709 Souri, A. H., Nowlan, C. R., Wolfe, G. M., Lamsal, L. N., Chan Miller, C. E., Abad, G. G., Janz, S. J., Fried, A., Blake, D. R.,
710 Weinheimer, A. J., Diskin, G. S., Liu, X., and Chance, K.: Revisiting the effectiveness of HCHO/NO₂ ratios for inferring
711 ozone sensitivity to its precursors using high resolution airborne remote sensing observations in a high ozone episode during
712 the KORUS-AQ campaign, *Atmos. Environ.*, 224, 117341, <https://doi.org/10.1016/j.atmosenv.2020.117341>, 2020.
- 713 Souri, A. H., Chance, K., Sun, K., Liu, X., and Johnson, M. S.: Dealing with spatial heterogeneity in pointwise-to-gridded- data
714 comparisons, *Atmos. Meas. Tech.*, 15, 41–59, <https://doi.org/10.5194/amt-15-41-2022>, 2022.
- 715 Souri, A. H., Johnson, M. S., Wolfe, G. M., Crawford, J. H., Fried, A., Wisthaler, A., Brune, W. H., Blake, D. R., Weinheimer, A.
716 J., Verhoelst, T., Compernelle, S., Pinardi, G., Vigouroux, C., Langerock, B., Choi, S., Lamsal, L., Zhu, L., Sun, S., Cohen,
717 R. C., Min, K.-E., Cho, C., Philip, S., Liu, X., and Chance, K.: Characterization of errors in satellite-based HCHO/NO₂
718 tropospheric column ratios with respect to chemistry, column-to-PBL translation, spatial representation, and retrieval
719 uncertainties, *Atmos. Chem. Phys.*, 23, 1963–1986, <https://doi.org/10.5194/acp-23-1963-2023>, 2023a.
- 720 Souri, A. H., Kumar, R., Chong H., Golbazi, M., Knowland, K. E., Geddes, J., and Johnson, M. S.: Decoupling in the vertical
721 shape of HCHO during a sea breeze event: The effect on trace gas satellite retrievals and column-to-surface translation,
722 *Atmospheric Environment*, 309, <https://doi.org/10.1016/j.atmosenv.2023.119929>, 2023b.
- 723 Spurr, R. J. D.: VLIDORT: a linearized pseudo-spherical vector discrete ordinate radiative transfer code for forward model and
724 retrieval studies in multilayer multiple scattering media, *J. Quant. Spectrosc. Rad. Trans.*, 102, 316–421,
725 <https://doi.org/10.1016/j.jqsrt.2006.05.005>, 2006.
- 726 Stewart, I. D. and Oke, T. R.: Local Climate Zones for Urban Temperature Studies, *B. Am. Meteorol. Soc.*, 93, 1879–1900,
727 <https://doi.org/10.1175/BAMS-D-11-00019.1>, 2012.
- 728 Tai, A., Martin, M., and Heald, C.: Threat to future global food security from climate change and ozone air pollution, *Nature Clim*
729 *Change*, 4, 817–821, <https://doi.org/10.1038/nclimate2317>, 2014.
- 730 Tao, M., Fiore, A. M., Jin, X., Schiferl, L. D., Commane, R., Judd, L. M., Janz, S., Sullivan, J. T., Miller, P. J., Karambelas, A.,
731 Davis, S., Tzortziou, M., Valin, L., Whitehill, A., Civerolo, K., and Tian, Y.: Investigating changes in ozone formation
732 chemistry during summertime pollution vents over the northeastern United States, *Environ. Sci. Technol.*, 56, 15312–15327,
733 <https://doi.org/10.1021/acs.est.2c02972>, 2022.
- 734 Tonnesen, G. S., and Dennis, R. L.: Analysis of radical propagation efficiency to assess O₃ sensitivity to hydrocarbons and NO_x:
735 2. Long-lived species as indicators of O₃ concentration sensitivity, *J. Geophys. Res. Atmos.*, 105, 9227–9241.
736 Doi:10.1029/1999JD900372, 2000.
- 737 US Environmental Protection Agency (US EPA): Air Quality Criteria for Ozone and Related Photochemical Oxidants (2006 Final),
738 U.S. Environmental Protection Agency, Washington, DC, EPA/600/R-05/004aF-cF, 2006.
- 739 Wang, W., van der A, R., Ding, J., van Weele, M., and Cheng, T.: Spatial and temporal changes of the ozone sensitivity in China
740 based on satellite and ground-based observations, *Atmos. Chem. Phys.*, 21, 7253–7269, [https://doi.org/10.5194/acp-21-7253-](https://doi.org/10.5194/acp-21-7253-2021)
741 2021, 2021.



- 742 Witte, J., Duncan, B., Douglass, A., Kurosu, T., Chance, K., and Retscher, C.: The unique OMI HCHO NO₂ feature during the
743 2008 Beijing Olympics: Implications for ozone production sensitivity, *Journal: Atmospheric Environment*, 45, 3103–3111,
744 <https://doi.org/10.1016/j.atmosenv.2011.03.015>, 2011.
- 745 Wu, S., Duncan, B. N., Jacob, D. J., Fiore, A. M. and Wild, O.: Chemical nonlinearities in relating intercontinental ozone pollution
746 to anthropogenic emissions, *Geophys. Res. Lett.*, 36, L05806, doi:10.1029/2008GL036607, 2009.
- 747 Zhang, L., Jacob, D. J., Kopacz, M., Henze, D. K., Singh, K., and Jaffe, D. A.: Intercontinental source attribution of ozone pollution
748 at western U.S. sites using an adjoint method, *Geophys. Res. Lett.*, 36, L11810, <https://doi.org/10.1029/2009GL037950>, 2009.
- 749 Zhu, L., Jacob, D. J., Kim, P. S., Fisher, J. A., Yu, K., Travis, K. R., Mickley, L. J., Yantosca, R. M., Sulprizio, M. P., De Smedt,
750 I., González Abad, G., Chance, K., Li, C., Ferrare, R., Fried, A., Hair, J. W., Hanisco, T. F., Richter, D., Jo Scarino, A.,
751 Walega, J., Weibring, P., and Wolfe, G. M.: Observing atmospheric formaldehyde (HCHO) from space: validation and
752 intercomparison of six retrievals from four satellites (OMI, GOME2A, GOME2B, OMPS) with SEAC4RS aircraft
753 observations over the southeast US, *Atmos. Chem. Phys.*, 16, 13477–13490, <https://doi.org/10.5194/acp-16-13477-2016>,
754 2016.
- 755 Zhu, L., Jacob, D. J., Keutsch, F. N., Mickley, L. J., Scheffe, R., Strum, M., González Abad, G., Chance, K., Yang, K.,
756 Rappenglück, B., Millet, D. B., and Baasandorj, M.: Formaldehyde (HCHO) as a Hazardous Air Pollutant: Mapping surface
757 air concentrations from satellite and inferring cancer risks in the United States, *Environ. Sci. Technol.*, 51, 5650–5657,
758 <https://doi.org/10.1021/acs.est.7b01356>, 2017a.
- 759 Zhu, L., Mickley, L. J., Jacob, D. J., Marais, E. A., Sheng, J., Hu, L., González Abad, G., and Chance, K.: Long-term (2005–2014)
760 trends in formaldehyde (HCHO) columns across North America as seen by the OMI satellite instrument: Evidence of changing
761 emissions of volatile organic compounds, *Geophys. Res. Lett.*, 44, 7079–7086, <https://doi.org/10.1002/2017GL073859>,
762 2017b.
- 763 Zhu, L., González Abad, G., Nowlan, C. R., Chan Miller, C., Chance, K., Apel, E. C., DiGangi, J. P., Fried, A., Hanisco, T. F.,
764 Hornbrook, R. S., Hu, L., Kaiser, J., Keutsch, F. N., Permar, W., St. Clair, J. M., and Wolfe, G. M.: Validation of satellite
765 formaldehyde (HCHO) retrievals using observations from 12 aircraft campaigns, *Atmos. Chem. Phys.*, 20, 12329–12345,
766 <https://doi.org/10.5194/acp-20-12329-2020>, 2020.
- 767



768 **Tables**

769

770 **Table 1. Statistics of the correlation of OMI and AQS normalized trends for HCHO, NO₂, and FNRs for major**
 771 **cities in the US and the average of all cities in the US (USA) between 2005-2019. Slopes of the trends for each**
 772 **species are also provided.**

Cities	Corr. HCHO	Slope HCHO Obs.	Slope HCHO Model	Corr. NO ₂	Slope NO ₂ Obs.	Slope NO ₂ Model	Corr. FNR	Slope FNR Obs.	Slope FNR Model
New York	0.01	0.10	0.05	0.91	-0.21	-0.20	0.78	0.20	0.20
Los Angeles	-0.01	-0.14	0.14	0.98	-0.21	-0.22	0.84	0.17	0.22
Chicago	NaN	NaN	0.07	0.91	-0.22	-0.21	NaN	NaN	0.18
Washington DC	0.38	0.11	0.05	0.89	-0.19	-0.20	0.77	0.18	0.21
Pittsburg	0.51	0.06	0.10	0.64	-0.21	-0.16	0.55	0.22	0.16
Atlanta	NaN	NaN	-0.07	0.33	-0.01	-0.17	NaN	NaN	0.18
Houston	0.40	-0.18	-0.06	0.79	-0.17	-0.17	-0.27	-0.12	0.13
USA	0.24	-0.05	0.15	0.98	-0.21	-0.20	0.91	0.21	0.21

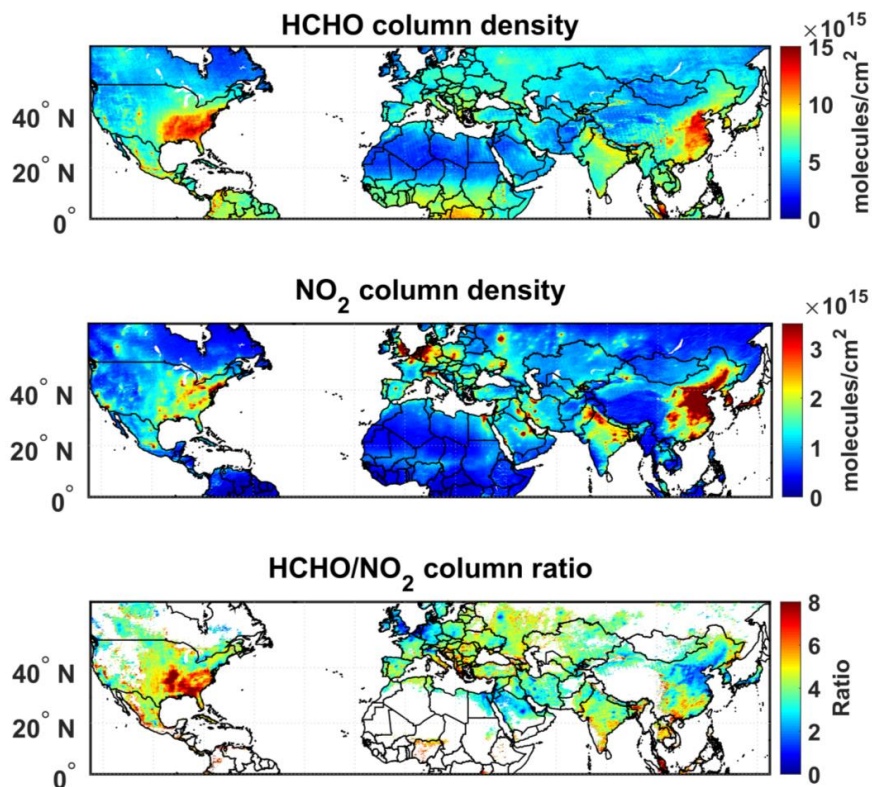
773 Correlation values are the correlation coefficient (R).

774 NaN values indicate cities where particular species data is not available for all years between 2005-2019.

775



776 **Figures**



777

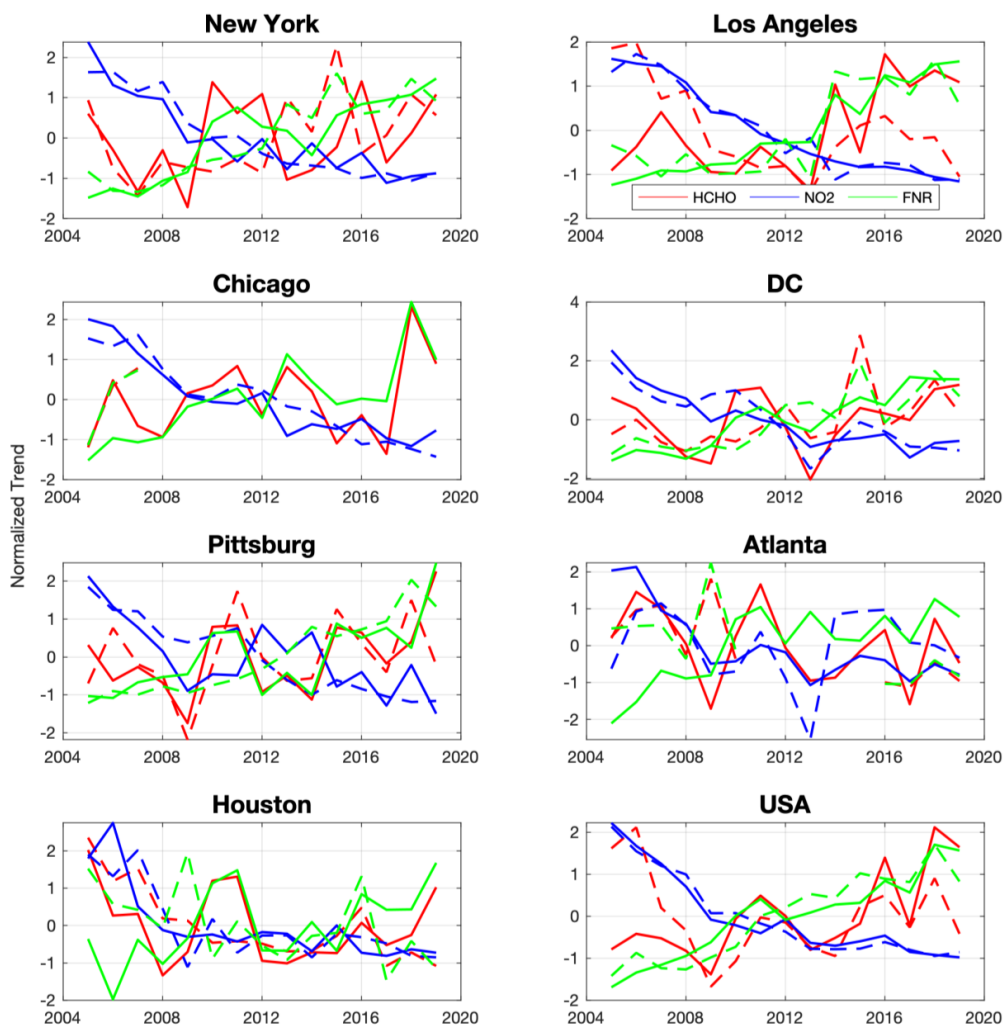
778

779

780

781

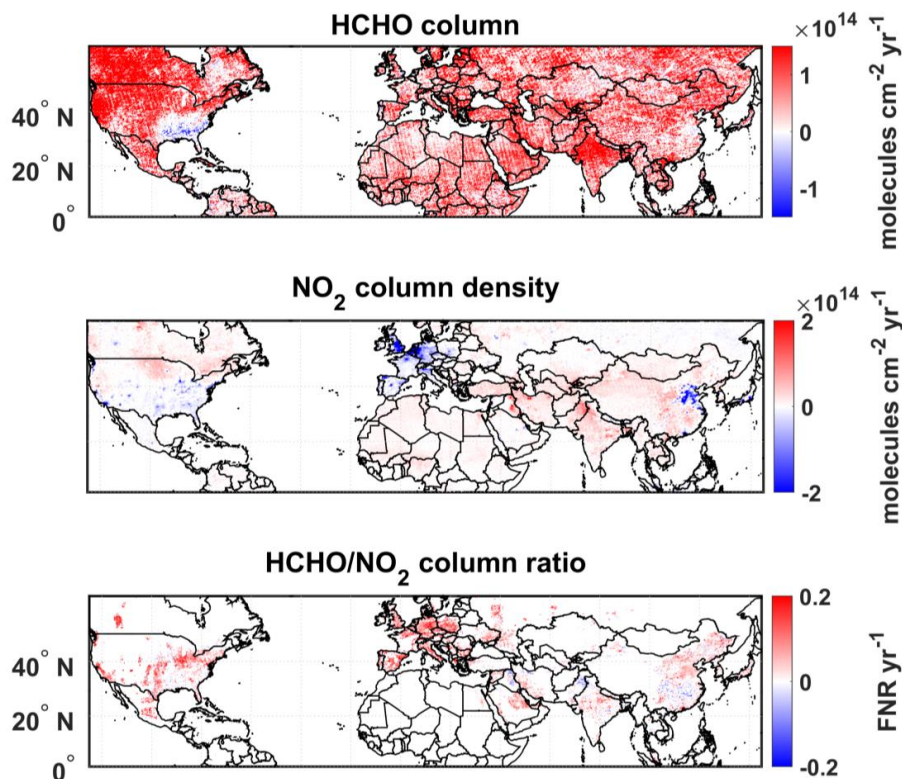
Figure 1: OMI-derived multi-year (2005-2021) summer mean (June-August) HCHO VCDs (top row), NO₂ VCDs (middle row), and resulting VCD FNRs at 0.1° × 0.1° latitude × longitude grid cells. Values of FNRs are displayed only for polluted regions (NO₂ VCD > 1.2 × 10¹⁵ molecule cm⁻²). The white color indicates data gaps or oceanic grid cells.



782

783 **Figure 2: Normalized time series (values from 2005 to 2019 normalized to 2005-2019 mean) of summer mean OMI HCHO**
784 **and NO₂ VCDs and column FNRs (solid lines). The same information is shown for surface concentrations from the EPA-**
785 **AQS in situ observations (dashed lines) over select cities and over all urban monitoring sites in the United States (bottom**
786 **right panel).**

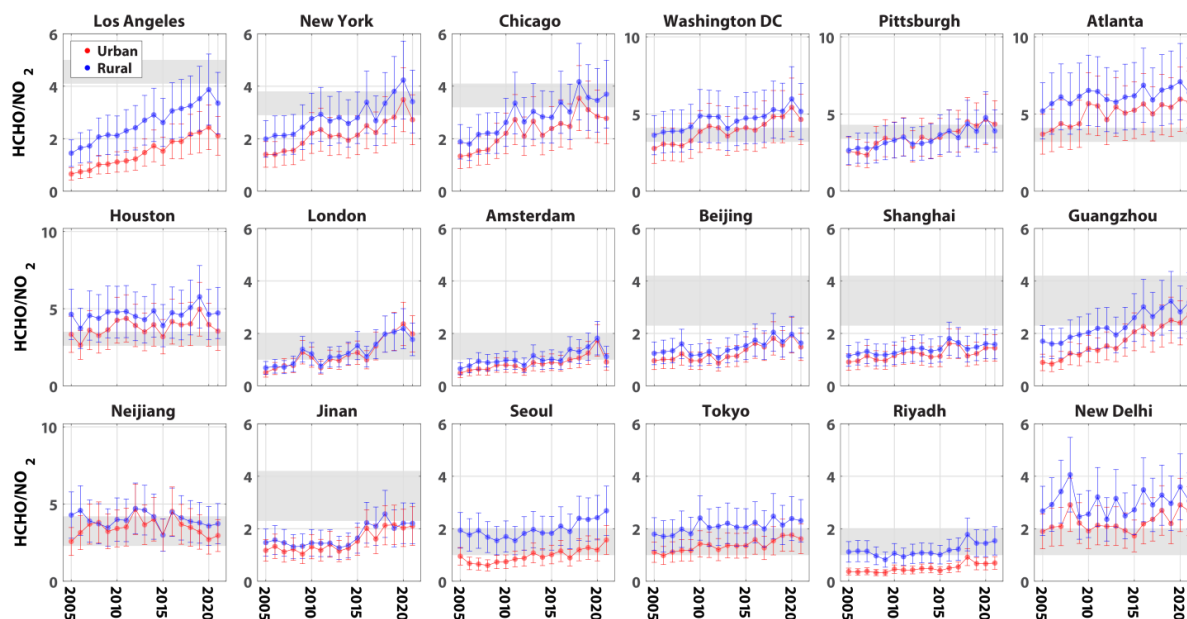
787



788

789 **Figure 3: OMI-derived trends in summer mean (June-August) time series of HCHO (top row) and NO₂ (middle row) VCDs**
790 **(units in molecule cm⁻² yr⁻¹), and corresponding FNR values (bottom row; unitless yr⁻¹) at 0.1° × 0.1° latitude × longitude**
791 **grid cells between 2005 and 2021. Values in the bottom row are displayed only for polluted regions (OMI NO₂ VCD > 1.2**
792 **× 10¹⁵ molecule cm⁻²). The white color indicates data gaps or oceanic grid cells. All trend values that are displayed are at**
793 **an 85% confidence level (p ≤ 0.15) for better visualization of spatial trend variability. Figure S1 shows the trend values at**
794 **99% confidence level and for all grid cells.**

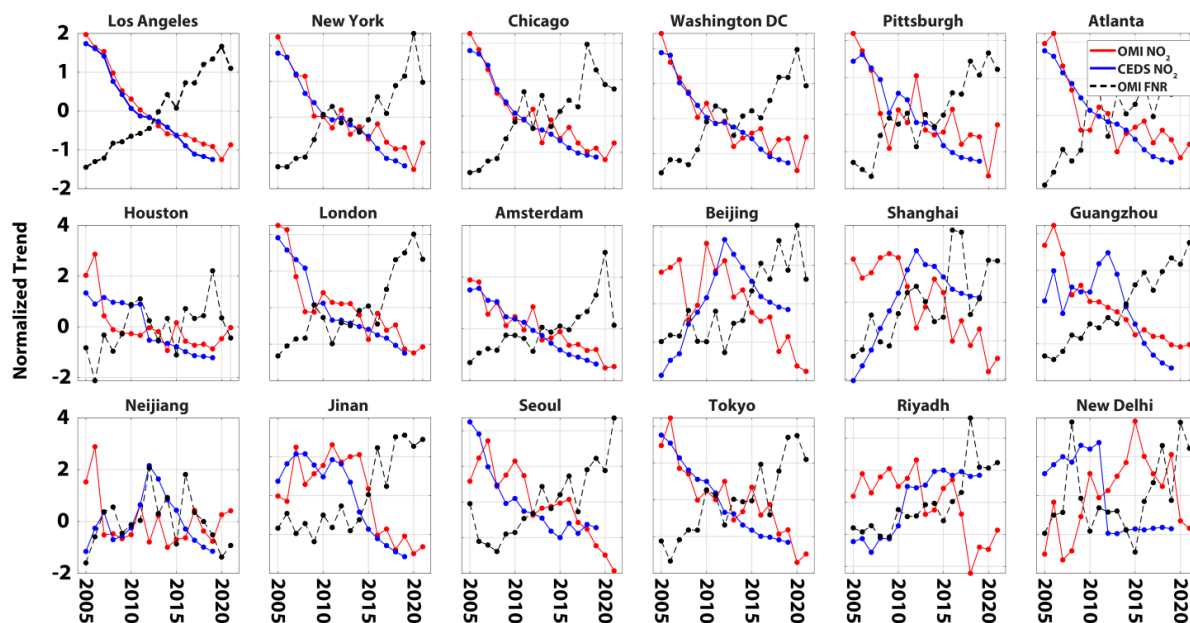
795



796

797 **Figure 4: Time series of OMI-derived summer mean (June-August) FNR VCD values for 18 selected cities across the North**
 798 **Hemisphere from 2005 to 2021. The different colors illustrate mean FNR values for urban (red) and rural areas around**
 799 **each city (blue). Grey shaded areas represent the transition zone of ozone production sensitivity regime threshold values**
 800 **as suggested by Jin et al. (2020) (cities in United States: Los Angeles, New York, Chicago, Washington DC, Pittsburgh,**
 801 **Atlanta and Houston), Wang et al. (2021) (cities in China: Beijing, Shanghai, Guangzhou, Neijiang and Jinan), and Duncan**
 802 **et al. (2010) (other cities). For interpretation, FNR values that are less than the transition zone have O₃ production which**
 803 **is VOC-limited and FNR values larger than the transition zone have O₃ production which is NO_x-limited.**

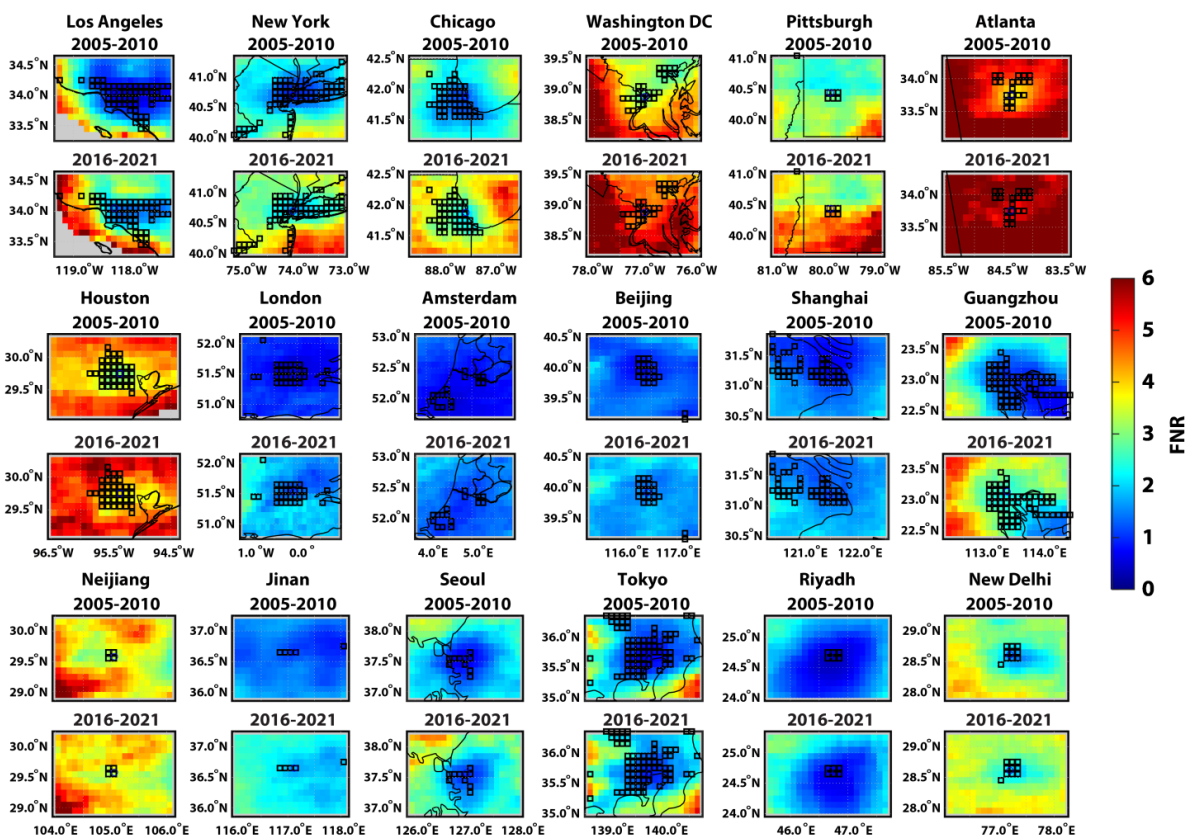
804



805

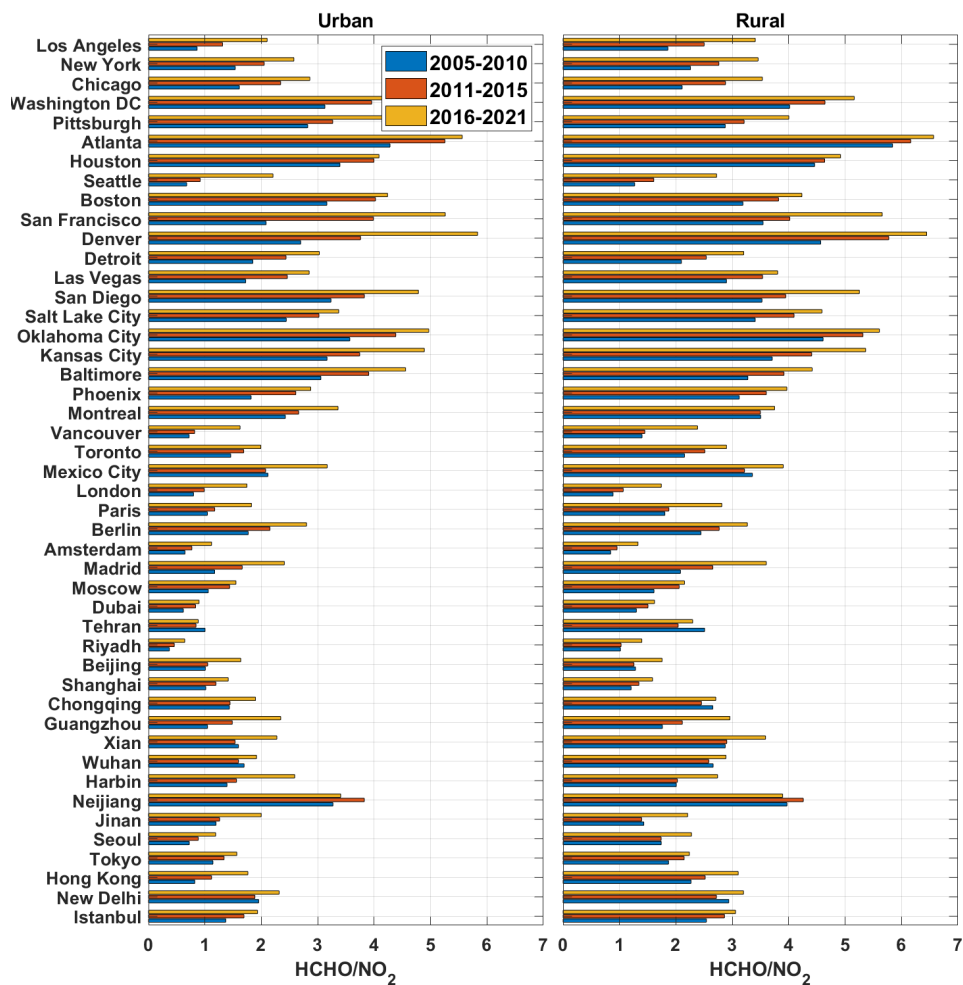
806 **Figure 5: Time series of normalized OMI-derived summer mean (June-August) VCD NO₂ and FNR trend values and**
807 **corresponding trends in anthropogenic emission of NO_x from the CEDS bottom-up inventory over the selected 18 cities**
808 **across the Northern Hemisphere from 2005 to 2021. CEDS emissions data is only displayed until 2019 due to this being the**
809 **most recent year of availability.**

810



811

812 **Figure 6: OMI-derived summer mean (June-August) FNR VCD values for 18 selected cities across the Northern**
813 **Hemisphere during 2005-2010 and 2016-2021. Outlined black squares represent CGLZ urban defined grid points. Grey**
814 **color indicates data gaps or oceanic grid cells.**



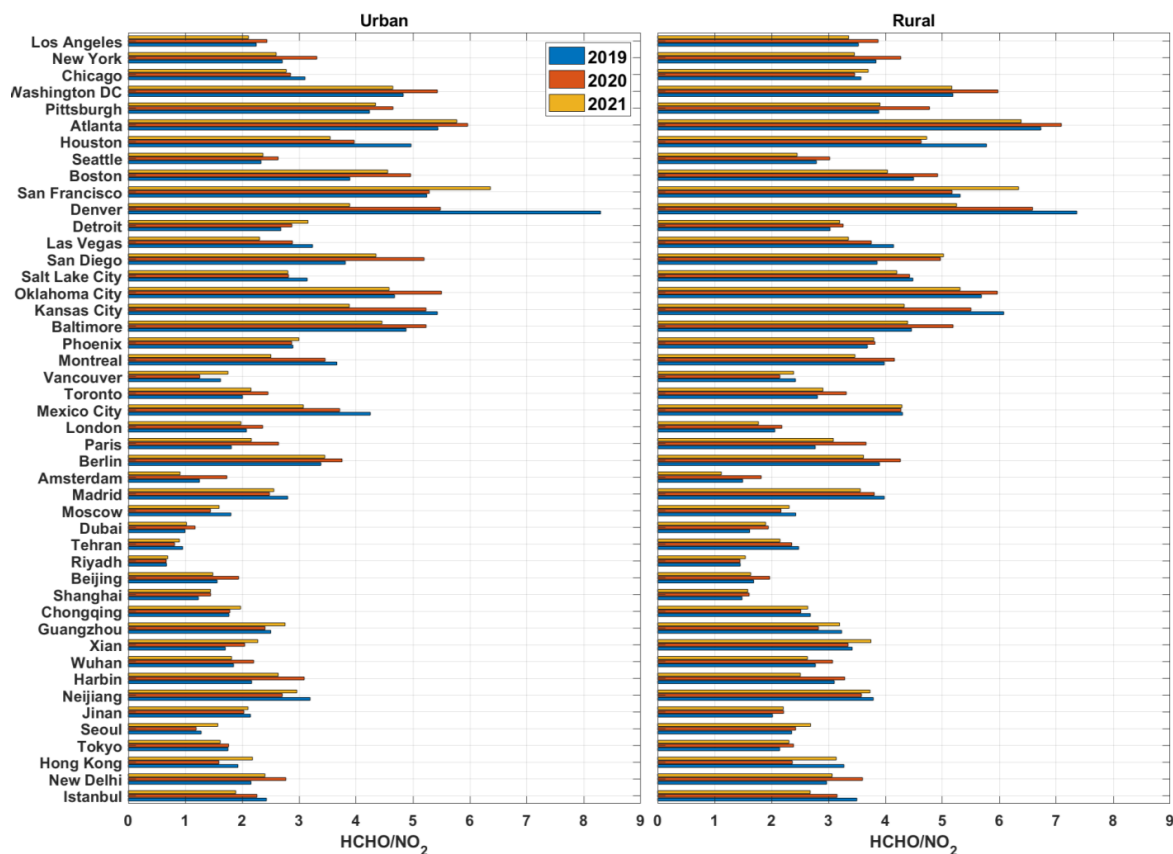
815

816 **Figure 7: OMI-derived summer-mean (June-August) FNR VCD values for a select 46 cities across the Northern**

817 **Hemisphere during 2005-2010 (blue), 2011-2015 (red) and 2016-2021 (orange). Each column represents mean ratio values**

818 **for urban city (left column) and the surrounding rural areas (right column).**

819



820

821

822

823

824

Figure 8: OMI-derived summer-mean (June-August) FNR VCD values for a select 46 cities across the Northern Hemisphere during 2019 (blue), 2020 (red) and 2021 (orange). Each column represents mean FNR values for urban city areas (left column) and the surrounding rural regions (right column).